Soft Matter

RSC Publishing

PAPER

Buckling pathways in spherical shells with soft spots

Jayson Paulose*[a] and David R. Nelson[b]

Cite this: *Soft Matter*, 2013, **9**, 8227

Received 13th March 2013
Accepted 13th May 2013

DOI: 10.1039/c3sm50719j

www.rsc.org/softmatter

Thin elastic spherical shells are known to exhibit a buckling instability at a finite external pressure. We study how this buckling is influenced by a weak region in an otherwise uniform shell, focusing on the case of a single small circular soft spot that is thinner than the rest of the shell. Using numerical simulations and theoretical arguments, we show that the soft region fundamentally alters the buckling behavior of the shell. The soft spot influences both the pressure at which the shell buckles, and the postbuckling shape of the shell. Depending on the properties of the soft spot, we find either a single buckling transition or two separate transitions as the external pressure is increased. We analyze the dependence of these buckling transitions on the size and thickness of the soft region. Besides contributing to our fundamental understanding of buckling transitions in inhomogeneous shells, our results can be applied to designing capsules with tunable shapes.

I Introduction

Buckling is a ubiquitous phenomenon in thin-walled elastic structures, such as plates and shells.[1,2] A prototypical example is the buckling transition of a thin spherical shell under pressure. Under an increasing external pressure, idealized shells without imperfections remain spherical until a threshold pressure is reached at which the shell buckles: at this point, a very small increment in pressure triggers a large deformation in the form of one or more indentations that significantly reduce the enclosed volume. Significant hysteresis is associated with this transition. In this sense, the buckling of shells in three dimensions resembles a first order phase transition, and the critical buckling pressure represents a limit of metastability. The situation is quite different for pressurized *rings* in two dimensions (or pressurized cylinders), where the behavior at buckling resembles a continuous phase transition (see, *e.g.* ref. 3). Understanding and mitigating buckling has long been important to engineers to prevent the catastrophic failure of macroscopic shell structures such as water tanks and submarines.[4] More recently, the buckling of thin spherical shells has been exploited for various functions, such as the measurement of shell elastic constants,[5] controlled release of encapsulated chemicals,[6] and mass-production of colloids with non-spherical, functional shapes.[7,8]

Whether buckling is desirable or avoidable, inhomogeneities in the shell, *i.e.* variations in the shape, thickness or material properties, strongly influence the buckling behavior. For instance, even small deviations from the perfect spherical shape induce shells to buckle at significantly reduced pressures, requiring engineers to build shells several times stiffer than their theoretical design specification to withstand a particular load.[9,10] Thermally excited shape fluctuations, which may be significant for shells with nanoscale thicknesses, also markedly reduce the buckling pressure.[11] The pollen grains of certain plant species, which can be modeled as elastic shells, have evolved one or more carefully shaped soft sectors in the otherwise stiff shell that guide their shape change as they dry out to evade the hysteresis associated with sudden buckling behavior.[12] Placing circular soft regions in specific geometric configurations on spherical shells also fundamentally alters their buckling under pressure, allowing them to shrink by about half their volume while retaining their spherical shape.[13] A recent study of spherical microcapsules whose thickness varied with latitude showed that the thickness inhomogeneity affects the buckling pressure, dynamics and postbuckling shapes.[14]

These studies are only beginning to explore the rich variety of shell inhomogeneities that may be exploited to control and extend buckling behavior, ranging from naturally occurring rafts and domains in multicomponent vesicles[15,16,17] to carefully tuned variations in shell shape, thickness and composition *via* microfluidic[18] and rapid prototyping[13,19] techniques. Understanding the effect of inhomogeneity on the buckling transition, besides being a challenging problem due to the highly nonlinear nature of large deflections in shells, has the potential to uncover new ways of using buckling to provide form and function. In this work, we study the effect of a previously unexplored inhomogeneity that is simple, yet general: a soft spot with a circular boundary in an otherwise uniform spherical shell. We use numerical simulations and theoretical arguments to understand the buckling and postbuckling behavior as the spot size and stiffness are varied. The response of the shell may be broken down into the response of the soft region and the response of the remainder of the shell; the interplay of these responses plays a significant role in explaining the observed behavior.

[a]*Harvard School of Engineering and Applied Sciences, Cambridge, MA 02138, USA. E-mail: jpaulose@post.harvard.edu*

[b]*Department of Physics, Harvard University, Cambridge, MA 02138, USA*

Our numerical model is similar to ones used in other studies of the buckling of both uniform[20] and nonuniform[12,14] shells under pressure. Our theoretical analysis builds on previous work both on uniform and slightly imperfect spherical shells,[10,21] and on the buckling of spherical *caps i.e.* shallow sections of spheres, with various boundary conditions.[22,23]

The rest of this paper is structured as follows: we introduce the elastic energy used to describe deformations in thin spherical shells, and identify the dimensionless quantities that are relevant for our description. We then present our numerical results from simulations of buckling shells under external pressure, and describe different buckling pathways that arise as the parameters are changed. To explain our numerical observations, we analyze the underlying continuum shell theory equations for a soft spot embedded in the rest of the shell. To provide context, we recap the buckling behavior of uniform shells, which provides much insight on the buckling of shells with soft spots. We then consider separately the deformations of the cap, and of the remainder of the shell, using scaling arguments and approximations to understand the underlying nonlinear differential equations that describe stresses and deformations in the shell. Finally we describe the hysteresis properties of the inhomogeneous shells when the pressure is cyclically varied, which is strongly influenced by the soft region. We conclude with potential applications and possible avenues for further research.

II Elastic theory of thin spherical shells

Typically, the elastic energy of deforming a three-dimensional (3D) object made up of a uniform elastically isotropic material depends on the detailed elastic strains at each point within the object and the 3D elastic Young's modulus E that relates strains to stresses. However, a simplification can be made for elastic *plates* and *shells*, structures which have a very small extent in one of the three spatial dimensions.[1,2] Then, it is sufficient to consider the deformation of the middle surface, a two-dimensional manifold. The elastic energy can be described using in-surface strains, which carry an energy penalty set by a two-dimensional (2D) Young's modulus Y, and changes in curvature of the middle surface, penalized by a bending rigidity κ. In terms of the 3D elastic modulus E and Poisson ratio ν of the material making up the shell, the 2D moduli are

$$Y = Eh, \tag{1}$$

$$\kappa = \frac{Eh^3}{12(1-\nu^2)}, \tag{2}$$

where h is the shell thickness. As a result, the thickness of the shell strongly affects its elastic response. In particular, for extremely thin plates and shells, the h^3-dependence of κ shows that bending is highly favoured over stretching, as demonstrated by the ease of bending a piece of paper compared to stretching it.

Whereas thin, flat elastic plates can exhibit pure bending deformations with no associated in-plane stretching and consequently a very low energy cost (the aforementioned sheet of paper being an example), the same is not always true of *shells* which are curved in their undeformed state. In flat plates, the contribution of normal (out-of-plane) deformations of the mid-surface to the in-plane strain is quadratic in the deformation, whereas the contribution to the bending tensor is linear. As a result, the bending energy dominates the elastic penalty of normal deformations of flat plates. In contrast, the underlying curvature of a shell mediates a *linear* coupling between out-of-plane displacements and in-plane strains: any transverse deformation ζ introduces a strain of order ζ/R, where R is the radius of curvature of the shell in its ground state.[1] Thus, bending and stretching are intimately coupled in curved shells, unlike elastic plates and membranes which are flat in the ground state.

An important consequence of this coupling is that normal deformations tend to be localized to narrow widths in spherical shells. A scaling analysis of the energy density reveals a length scale that sets the extent of characteristic deformations, which is small compared to the shell radius. Consider a deformation of maximum depth ζ localized over a length l in the spherical shell, which has a corresponding curvature change of approximately ζ/l^2 and strain ζ/R. The bending energy per unit area of the deformation is $\kappa\zeta^2/l^4$ while the stretching energy per unit area is $Y\zeta^2/R^2$. Minimizing the sum of the bending and stretching energies with respect to l gives rise to a typical elastic length scale of localization of deformations for which the total elastic energy is minimized,

$$l = \ell \equiv \left(\frac{\kappa R^2}{Y}\right)^{1/4} \equiv \frac{R}{\gamma^{1/4}}, \tag{3}$$

where we have introduced the dimensionless *Föppl–von Kármán number*,

$$\gamma \equiv \frac{YR^2}{\kappa} \approx 10\left(\frac{R}{h}\right)^2. \tag{4}$$

The Föppl–von Kármán number quantifies the relative importance of stretching to bending for spherical shells. It is large for thin elastic shells. Typically, a shell is considered thin, *i.e.* the abstraction to a two-dimensional surface is valid and shell theory can be used, when $h \lesssim 0.1R$; *i.e.*, $\gamma \gtrsim 1000$. Very large Föppl–von Kármán numbers are common in both natural and artificial systems. For instance, the radius of a ping-pong ball is about 100 times its wall thickness, leading to $\gamma \approx 10^5$. Typical values for the elastic moduli and radius of curvature of a red blood cell[24] lead to estimates for γ in the range 10^4 to 10^5. Therefore, typical deformations vary over a length scale ℓ that is much smaller than the radius of the shell. This separation of scales simplifies the theoretical analysis of deformations of spherical shells.

A Elastic energy of thin shells

We use the standard Kirchhoff–Love description of thin elastic shells, in which the elastic energy density of the surface is quadratic in two-dimensional strain and curvature tensors.[25]

The elastic energy is the sum of a stretching and a bending component,

$$E = \int \mathrm{d}S \left[\frac{Y}{2(1-\nu^2)} \left((u_{11}+u_{22})^2 - 2(1-\nu)\left(u_{11}u_{22} - {u_{12}}^2\right) \right) + \frac{\kappa}{2} \left((k_{11}+k_{22})^2 - 2(1-\nu)\left(k_{11}k_{22} - {k_{12}}^2\right) \right) \right] \quad (5)$$

where the indices i, j label the local coordinate directions tangent to the shell mid-surface, u_{ij} is the 2×2 strain tensor and $k_{ij} = K_{ij} - K_{ij}^0$ the change in the curvature tensor K_{ij} from its initial value K_{ij}^0. The integration is carried out over the mid-surface of the shell. The stress and curvature tensors are defined to vanish when the external pressure vanishes—the equilibrium shape is a sphere of radius R. The initial curvature tensor K_{ij}^0 of the shell mid-surface is that of a sphere with radius R: $K_{ij}^0 = \delta_{ij}/R$ at every point for an orthonormal basis set up in the tangent plane to the sphere at that point.

This expression forms the basis of a discretized model of a thin shell appropriate for numerical simulation (see Appendix A). Upon picking a suitable coordinate system, rewriting the elastic energy expressions in terms of displacement fields and stress functions, and performing a functional extremization with respect to these fields, we obtain the equations of shell theory, which are nonlinear but amenable to analysis using numerical and approximate analytical methods. We use both numerical simulations and a theoretical analysis of the shell theory equations to understand the behavior of inhomogeneous shells.

B Shells with soft spots

In our study, we restrict ourselves to a specific inhomogeneity: a thin region with a circular boundary in an otherwise uniform spherical shell. By considering a small region that is softer than the rest of the shell, we open up the possibility of triggering an instability in the soft region before the shell as a whole collapses. (A stiffer region in the shell would affect the pressure at which the shell collapses, but would not show any additional instabilities before this collapse; we do not consider stiffer regions here.) The thin region, or *cap*, is assumed to be made of the same material as the rest of the shell (the *remainder*), but with a thickness $\tilde{h} < h$ where h is the uniform thickness of the remainder. The elastic moduli in the cap and the remainder are obtained using eqn (1) and (2) with the appropriate thicknesses; the cap is thus easier to bend and stretch than the shell. We treat the cap and the remainder as materially coupled to each other; *i.e.* the displacements, stresses and bending moments are continuous across the boundary between the cap and the shell.

In what follows, we will use $\tilde{Y}$, $\tilde{\kappa}$,… to refer to the properties of the cap and Y, κ,… for the remainder. Without loss of generality, we choose the soft cap to be centered at the north pole, and its size is then defined by the azimuthal angle α (in radians) subtended by its rim. We consider caps small compared to the rest of the shell ($\alpha \lesssim \pi/4$). The dimensionless parameters characterizing the shell are the Föppl–von Kármán number γ (computed using the elastic properties of the *remainder*), the cap–remainder thickness ratio $\tau \equiv \tilde{h}/h < 1$, and the dimensionless size $\lambda \equiv R\alpha/\ell = \alpha\gamma^{1/4}$ (which expresses the radial size of the cap in units of the elastic length scale ℓ of the remainder). Alternatively, one could use the Föppl–von Kármán number and elastic length scale of the cap, which are simply related to the remainder quantities *via* $\tilde{\gamma} = \gamma/\tau^2 > \gamma$, $\tilde{\ell} = \ell\sqrt{\tau} < \ell$.

III Numerical results

We numerically simulate the buckling of shells with soft spots under hydrostatic pressure. We restrict ourselves to a single inhomogeneity in the form of a region with a circular boundary that is thinner than the rest of the shell. In buckling simulations, the pressure is measured in units of the classical buckling pressure $p_0 = 4\sqrt{\kappa Y}/R^2$ of a *uniform* shell[2] with the same thickness as the remainder (see Section V for more details on the buckling transition for uniform spherical shells).

In a typical simulation, a uniform pressure p is exerted on the shell by adding a volume integral $p\int \mathrm{d}V$ to eqn (5), and the local equilibrium configuration of the shell is computed. More generally, p would be the pressure difference between the inside and the outside of the shell; if the shell contains a fluid such as air or water, we assume that it is permeable to the enveloped fluid, thus allowing reductions in volume in response to the pressure. (An experimental realization is the osmotic crushing of suspensions of droplet-templated microcapsules that are permeable to the inner and outer fluid but not to solute ions; introducing a solute into the outer phase exerts an osmotic pressure on the capsules which can shrink in response by releasing their enclosed fluid.[14]) The pressure is initially set to zero, and incremented by a small amount between successive equilibrations. Fig. 1 shows the outcome of a simulation on a shell with Föppl–von Kármán number $\gamma = 10^4$, thickness ratio $\tau = 0.4$, and dimensionless spot size $\lambda = 5.2$. At early stages (low pressures) the shell responds *via* a near-uniform contraction while maintaining a roughly spherical shape. At a critical value of the pressure, which we call p_{c_1}, the cap experiences a snap-through transition to an inverted shape, although the rest of the shell remains spherical. This shape persists until a higher

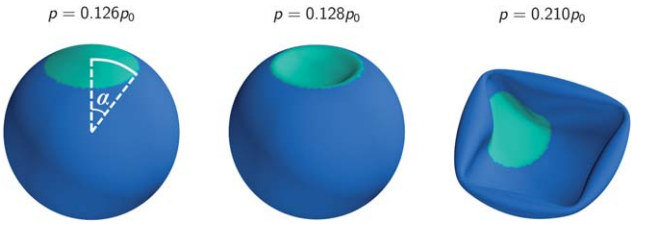

Fig. 1 Results of a buckling simulation on a shell with $\gamma = 10^4$, $\tau = 0.4$ and cap size $\alpha = 0.52$ (where α is the azimuthal angle subtended by the spot at the center of the undeformed spherical shape), corresponding to $\lambda = R\alpha/\ell = 5.2$. Equilibrium configurations at different pressures, measured in units of the classical buckling pressure of a uniform shell without the soft spot, are shown. The mesh points in the soft region are colored differently from the remainder. The shape of the shell is spherical up to the first buckling pressure $p_{c_1} = 0.128p_0$, when the soft cap snaps through to an inverted shape. This shape is largely unchanged up to the second, more catastrophic buckling event at $p_{c_2} = 0.21p_0$.

critical pressure p_{c_2} is reached, at which point the rest of the shell experiences a catastrophic collapse. In real shells, this collapse would be terminated by self-contact of the shell; in our simulations, we introduce a minimum volume restriction of roughly 10% of the original volume to stabilize the collapsed shape, as it is computationally simpler to implement than self-avoidance. For this particular set of parameters, $p_{c_1} = 0.128p_0$ and $p_{c_2} = 0.21p_0$.

This buckling pathway, with two distinct buckling events as the pressure is ramped up, is observed over a wide range of values of τ and λ. For future reference, we will call this pathway I. However, for other parameter ranges, different behavior is observed. For modestly thinned caps such that $\tau \gtrsim 0.6$, practically all shells only display *one* buckling transition, a catastrophic collapse from a spherical shape to a fully deflated shape similar to the final shape in Fig. 1 without any intermediate range of pressures where only the cap has snapped through. We refer to this as pathway II. There is also a narrow range of parameters, for small values of τ and λ, in which a deformation is observed in the cap before the rest of the shell buckles, but the deformation is a smooth and continuous inversion of the shell as the pressure rises, rather than a sudden snap-through at a particular pressure. For these shells, the collapse of the rest of the shell still happens when a particular pressure is reached. This is termed pathway III in what follows. For both pathway II and pathway III, p_{c_1} refers to the critical pressure at which the lone buckling event occurs, and p_{c_2} is undefined.

Fig. 2 summarizes the various buckling pathways for shells with different thickness ratios τ as a function of the dimensionless size $\lambda = \alpha\gamma^{1/4}$ of the soft spot. These results are independent of γ for small spots, as will be shown in the theoretical analysis below. We observe that when the soft spot is extremely thin compared to the rest of the shell ($\tau < 0.5$), pathway I is almost always observed: two distinct buckling events occur at pressures p_{c_1} and p_{c_2}, and there is a range of pressures $p_{c_1} < p < p_{c_2}$ over which the cap has experienced snap-through buckling but the shell is stable against further collapse. The exception is for extremely small spots ($\lambda \lesssim 1.5$) where buckling occurs *via* pathway III with a continuous deformation of the cap from its initial shape to a fully inverted shape, followed by a single catastrophic buckling event at a pressure p_{c_1}. For less drastic thickness changes ($\tau \geq 0.6$), pathway II is almost exclusively observed, *i.e.* a single catastrophic buckling event induces collapse of the entire shell, with no significant deviation from the spherical shape prior to buckling. For $\tau = 0.5$, pathway I is observed in a narrow range of spot sizes $1.5 < \lambda < 3.5$, and pathway II is observed outside this range. Note that, even when the cap size shrinks to zero ($\lambda \to 0$) the critical buckling pressure remains smaller than p_0, the buckling pressure of an ideal shell, due to inevitable small scale inhomogeneities introduced by the amorphous mesh that describes the shell (see Appendix A).

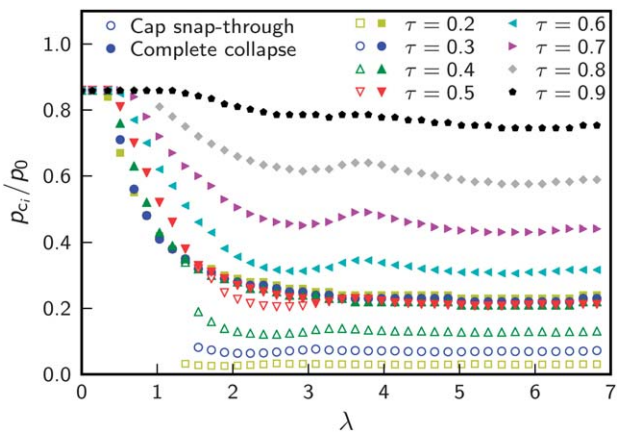

Fig. 2 Buckling pressures p_{c_1} and p_{c_2} of the first and second buckling events as the pressure is ramped up in numerical simulations, as a function of rescaled cap size for a variety of thickness ratios $\tau = \tilde{h}/h$. The pressure is rescaled by the classical buckling pressure p_0 of a sphere with the same properties as the remainder. In all cases, $\gamma = 10^4$, although the results when expressed with rescaled variables are largely insensitive to γ. Empty symbols signify a snap-through transition localized to the cap, whereas filled symbols signify catastrophic collapse of the entire shell. Some shells exhibit two distinct buckling events—snap-through of the cap at the lower pressure p_{c_1} and collapse of the rest of the shell at the higher pressure p_{c_2}. Other shells display only a single transition, which is always a catastrophic collapse of the whole shell, at the first buckling pressure p_{c_1}. The second buckling pressure p_{c_2} is not defined for these shells.

As expected, the snap-through buckling of the cap happens at higher pressures for thicker (*i.e.* stiffer) caps. However, for shells following pathway I ($0.2 \leq \tau \leq 0.5$), the pressure p_{c_2} at which the whole shell collapses has a very weak dependence on the thickness ratio τ. Except for some small deviations at small λ, the pressure of bulk collapse for these thickness ratios seems to follow a near-universal curve of p/p_0 as a function of λ. This trend is in contrast to shells following pathway II ($\tau > 0.5$), for which the pressure associated with large-scale collapse of the shell *does* depend strongly on τ. We also notice an interesting common structure in the p_{c_1} *vs.* λ curves for different thickness ratios, all of which have a distinctive concave-upwards shape with strong variations up to a spot size $\lambda \sim 3$–4 beyond which they level off to a roughly constant value that depends on τ.

To explain these features of the critical pressure function defined by $p = p_{c_1}(\lambda,\tau)$ and $p = p_{c_2}(\lambda,\tau)$, we analyze the various mechanisms that bring about the elastic buckling instability in the following sections.

IV Governing equations of shell theory

We begin by summarizing the equations governing the stresses and strains of elastic spherical shells. Initially, we consider completely uniform shells. For theoretical analysis, we use *shallow shell theory*,[2,25] where we consider a section of the shell small enough so that slopes relative to a tangent plane at the basal point are small. Then, we set up a Cartesian coordinate system (x,y) in this tangent plane, and describe deformations of the shell in terms of tangential displacement fields $U(x,y)$, $V(x,y)$ and the normal displacement $W(x,y)$. The nonlinear strain tensor is related to the displacements *via*[2,25]

$$u_{xx} = U_{,x} + \frac{1}{2}W_{,x}{}^2 - \frac{W}{R}, \tag{6}$$

$$u_{yy} = V_{,y} + \frac{1}{2}W_{,y}{}^2 - \frac{W}{R}, \tag{7}$$

$$u_{xy} = \frac{1}{2}\left(U_{,y} + V_{,x} + W_{,x}W_{,y}\right), \tag{8}$$

where we use the notation $f_{,\alpha} \equiv \partial_\alpha f$ for spatial derivatives. The curvature tensor is approximately

$$k_{ij} = W_{,ij}. \tag{9}$$

The total energy, including the elastic contribution [eqn (5)] as well as the contribution due to a finite external pressure p, reduces to

$$E_{\mathrm{tot}} = \int \mathrm{d}x\mathrm{d}y \left[\frac{Y}{2(1-\nu^2)}\left(\left(u_{xx}+u_{yy}\right)^2 - 2(1-\nu)\left(u_{xx}u_{yy} - {u_{xy}}^2\right)\right) + \frac{\kappa}{2}\left(\left(W_{,xx}+W_{,yy}\right)^2 - 2(1-\nu)\left(W_{,xx}W_{,yy} - {W_{,xy}}^2\right)\right) - pW\right]. \tag{10}$$

Equilibrium shapes of the shell section correspond to fields U, V and W for which the energy functional, eqn (10), is stationary. Extremizing E_{tot} with respect to variations in U, V and W gives rise to three nonlinear differential equations:

$$\kappa\nabla^4 W - \frac{1}{R}\left(\sigma_{xx}+\sigma_{yy}\right) - \left(\sigma_{xx}W_{,x} + \sigma_{xy}W_{,y}\right)_{,x} - \left(\sigma_{xy}W_{,x} + \sigma_{yy}W_{,y}\right)_{,y} = p, \tag{11}$$

$$\sigma_{xx,x} + \sigma_{xy,y} = 0, \tag{12}$$

$$\sigma_{xy,x} + \sigma_{yy,y} = 0, \tag{13}$$

where $\nabla^2 f = f_{,xx} + f_{,yy}$, $\nabla^4 f = \nabla^2(\nabla^2 f)$, and σ_{ij} is the 2D stress tensor, with components

$$\sigma_{xx} = \frac{Y}{1-\nu^2}\left(u_{xx} + \nu u_{yy}\right), \tag{14}$$

$$\sigma_{yy} = \frac{Y}{1-\nu^2}\left(u_{yy} + \nu u_{xx}\right), \tag{15}$$

$$\sigma_{xy} = \sigma_{yx} = \frac{Y}{1+\nu}u_{xy}. \tag{16}$$

Eqn (12) and (13) are automatically satisfied by introducing the Airy stress function χ, derivatives of which give the stress tensor:[1]

$$\sigma_{xx} = \chi_{,yy};\ \sigma_{yy} = \chi_{,xx};\ \sigma_{xy} = -\chi_{,xy}. \tag{17}$$

When σ_{ij} is written in terms of the Airy function, eqn (11) becomes

$$\kappa\nabla^4 W - \frac{1}{R}\nabla^2\chi - N_2(\chi, W) = p, \tag{18}$$

where

$$N_2(f,g) = f_{,xx}g_{,yy} + f_{,yy}g_{,xx} - 2f_{,xy}g_{,xy} \tag{19}$$

defines a second-order nonlinear differential operator. Although any choice of the function $\chi(x,y)$ automatically satisfies eqn (12) and (13), χ must also be related to real displacement fields U, V and W *via* eqn (14)–(16). Eliminating the fields U and V from these three equations reduces them to a single compatibility condition for χ:

$$\frac{1}{Y}\nabla^4\chi + \frac{1}{R}\nabla^2 W + \frac{1}{2}N_2(W, W) = 0. \tag{20}$$

Eqn (18) and (20), together with appropriate boundary conditions, govern the equilibrium deflections and stresses of a uniform shallow shell. The presence of the nonlinear operator makes solving the shallow shell equations subtle and challenging, but they are amenable to analysis through scaling arguments and numerical methods.

A Equations in polar coordinates

When dealing with shells with soft caps, it is advantageous to use polar coordinates r,θ rather than x,y, with the origin at the center of the soft region (so that $x = r\cos\theta$, $y = r\sin\theta$). In polar coordinates, the strain tensor reads

$$u_{rr} = U_{,r} - \frac{W}{R} + \frac{1}{2}{W_{,r}}^2, \tag{21}$$

$$u_{\theta\theta} = \frac{U}{r} + \frac{V_{,\theta}}{r} - \frac{W}{R} + \frac{1}{2}\left(\frac{W_{,\theta}}{r}\right)^2, \tag{22}$$

$$u_{r\theta} = \frac{1}{2}\left(\frac{U_{,\theta}}{r} + V_{,r} - \frac{V}{r} + \frac{W_{,r}W_{,\theta}}{r}\right), \tag{23}$$

the curvature tensor is

$$k_{rr} = W_{,rr}, \tag{24}$$

$$k_{\theta\theta} = \frac{W_{,r}}{r} + \frac{W_{,\theta\theta}}{r^2}, \tag{25}$$

$$k_{r\theta} = \frac{W_{,r\theta}}{r} - \frac{W_{,\theta}}{r^2}, \tag{26}$$

and stresses are given by

$$\sigma_{rr} = \frac{\chi_{,r}}{r} + \frac{\chi_{,\theta\theta}}{r^2};\quad \sigma_{\theta\theta} = \chi_{,rr};\quad \sigma_{r\theta} = \frac{\chi_{,\theta}}{r^2} - \frac{\chi_{,r\theta}}{r}. \tag{27}$$

The governing equations remain unchanged (eqn (18) and (20)) but with the differential operators

$$\nabla^2 f = f_{,rr} + \frac{f_{,r}}{r} + \frac{f_{,\theta\theta}}{r^2},\quad \nabla^4 f = \nabla^2\left(\nabla^2 f\right), \tag{28}$$

$$N_2(f,g) = f_{,rr}\left(\frac{g_{,r}}{r} + \frac{g_{,\theta\theta}}{r^2}\right) + g_{,rr}\left(\frac{f_{,r}}{r} + \frac{f_{,\theta\theta}}{r^2}\right) - 2\left(\frac{f_{,r\theta}}{r} - \frac{f_{,\theta}}{r^2}\right)\left(\frac{g_{,r\theta}}{r} - \frac{g_{,\theta}}{r^2}\right). \tag{29}$$

V Buckling of uniform spherical shells under pressure

In preparation for our analysis of nonuniform shells, we review here the buckling of *uniform* spherical shells under external pressure, following the approach in ref. 10. The classical

buckling of spherical shells can be understood using a linearized analysis of the shell equations.

Prior to buckling, a consideration of the forces on a section of the shell shows that the shell contracts uniformly by an amount $W_0 = pR^2(1-\nu)/2Et$ and is in a uniform state of compressive stress $\sigma_{xx} = \sigma_{yy} = -pR/2$, corresponding to an Airy stress function $\chi_0 = -pR(x^2+y^2)/4$. The buckling mode can be obtained by linearizing the nonlinear shell equations around this pre-stressed state. Upon substituting $W = W_0 + W_1$ and $\chi = \chi_0 + \chi_1$ in eqn (40) and keeping terms linear in the normal displacement W_1 and Airy function χ_1, we find:

$$\kappa\nabla^4 W_1 - \frac{1}{R}\nabla^2\chi_1 + \frac{pR}{2}\nabla^2 W_1 = 0, \tag{30}$$

$$\nabla^4\chi_1 + \frac{Y}{R}\nabla^2 W_1 = 0. \tag{31}$$

The nonlinear coupling between the pre-stress and the normal deflection *via* the term $N_2(\chi_0,W_1)$ is responsible for the last term on the left-hand side of eqn (30). We search for oscillatory solutions of the form $W_1 = Ae^{i\boldsymbol{q}\cdot\boldsymbol{x}}$, $\chi_1 = Be^{i\boldsymbol{q}\cdot\boldsymbol{x}}$ with some two-dimensional wavevector $\boldsymbol{q} = (q_x,q_y)$. Such a solution to eqn (30) and (31) can only exist provided

$$\kappa q^4 - \frac{pR}{2}q^2 + \frac{Y}{R^2} = 0, \tag{32}$$

with the requirement for oscillatory solutions being that the wavevector magnitude $q \equiv \sqrt{\boldsymbol{q}\cdot\boldsymbol{q}}$ is real and positive. The smallest value of p at which solutions with $q^2 > 0$ exist is $p = 4\sqrt{\kappa Y}/R^2 \equiv p_0$, and the corresponding wavevector magnitude of the solution that arises is $q = 1/\ell = \gamma^{1/4}/R$. This pressure is identified as the buckling pressure of the shell. Note that the instability would not exist without the coupling between χ_0 and W_1 mentioned above, and is a nonlinear effect even though it is captured by a linearized analysis.

The linearized buckling analysis shows that a uniform shell which contracts isotropically under low external pressures can release this compressive stress, at the cost of bending energy, by taking on an oscillatory transverse deflection. Such a deflection becomes energetically favorable at the pressure $p_0 = 4\sqrt{\kappa Y}/R^2$. In fact, there are many degenerate deflection modes that arise at this critical pressure, since all wavevectors $\boldsymbol{q}$ such that $q = |\boldsymbol{q}| = 1/\ell$ are allowed. The wavelength associated with these modes is $2\pi\ell = 2\pi R/\gamma^{1/4} \ll R$ since $\gamma \gg 1$ for thin shells. Thus, the buckling of spherical shells is triggered by one of many degenerate modes with wavelength much smaller than the shell radius.

We have not established here that the oscillatory modes that arise at the buckling pressure are unstable toward further growth. This can be done by evaluating higher order terms in the elastic energy associated with the modes (see *e.g.* ref. 2). We do not reproduce that calculation here, but instead present a qualitative argument for the ultimate fate of the shell at the buckling pressure, from ref. 1, which considers the energetics of inversions of sections of the shell. Thin spherical shells under pressure find it favorable to reduce their volume using nearly isometric inversions, which leave the metric within most of the inverted region unchanged and localize the elastic energy to the narrow rim of the inversion (which has a width of order ℓ). The energy associated with an inversion of depth d is characterized by a quantity we denote the Pogorelov energy,[1,26]

$$E_{\rm el} = c\kappa\gamma^{1/4}(d/R)^{3/2}, \tag{33}$$

where c is a dimensionless constant. If the shell is under external pressure p, the net energy including the work done by the pressure is $E = E_{\rm el} + p\Delta V$, where $\Delta V \sim -Rd^2$ is the volume change due to the inversion. We immediately see that at large values of inversion depth d, the second term dominates, and inversions can reduce their net energy by growing even deeper. The total energy $E(d)$ has a maximum when

$$\kappa\gamma^{1/4}\frac{d^{1/2}}{R^{3/2}} \sim pRd \Rightarrow \frac{d_{\max}}{R} \sim \left(\frac{\kappa}{pR^3}\right)^2\sqrt{\gamma}. \tag{34}$$

Therefore, for a particular pressure, inversions of depth $d > d_{\max}(p)$ grow uncontrollably, until some other constraint such as self-contact prevents further growth of the inversion. At the buckling pressure, $d_{\max}(p_0) \sim R/\sqrt{\gamma} \sim h$; thus, even an inversion of very small depth, comparable to the thickness h of the shell, is unstable to growth. Pogorelov's picture can be reconciled with the linear stability analysis sketched above as follows: the oscillatory buckling modes that arise at the buckling pressure can be thought of as many tiny inversions covering the entire sphere; any one of these inversions can grow uncontrollably, giving rise to the characteristic inverted shape of a buckled spherical shell. Thus the buckling mode is a transient, and the final buckled shape of the shell displays one or more large inversions that significantly reduce the enclosed volume of the shell, very similar to the final configuration in Fig. 1. These large inversions with depth comparable to the shell radius have additional features, such as the sharp points of stress focusing, that deviate from the Pogorelov isometric inversion, but the associated scaling of the elastic energy with depth is hardly changed.[27,28]

The transient buckling mode can only be observed in real shells by arresting its uncontrolled growth. This has been done for metallic thin shells by buckling a shell that encloses a solid ball of slightly smaller radius: the deformed shell contacts the inner ball when the buckling mode arises, arresting it so it can be visualized.[29] We can replicate this remarkable experiment in our simulations by including a steep repulsive potential within the mesh and ramping up the external pressure until the shell buckles, at which point the internal repulsive potential prevents the unstable mode from growing uncontrollably. The result is shown in Fig. 3, showing the small-wavelength buckling pattern that extends over the shell.

VI Snap-through of soft caps

We now turn to the shells with soft spots, numerically investigated in Section III. The radius of the soft spot, measured along a sphere geodesic, is $r_0 \equiv R\alpha$. We expect large changes in the buckling due to external pressure whenever $r_0 > \ell = R/\gamma^{1/4}$, the elastic length; *i.e.* $\lambda = (r_0/R)\gamma^{1/4} > 1$. Indeed, unless $\lambda \ll 1$, the soft spot will substantially influence the mechanics of the shell and, in particular, be the first region responding to

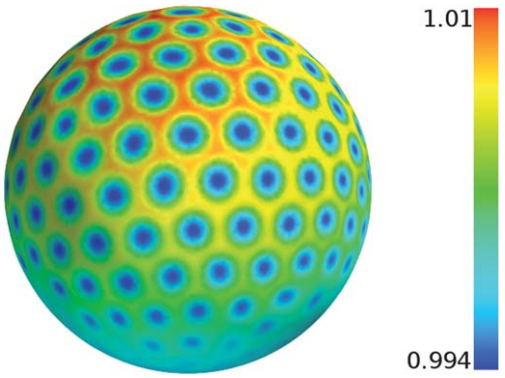

Fig. 3 Simulation of a uniform shell with large Föppl–von Kármán number ($\gamma = 10^6$) under an external pressure above the buckling transition, and an inner ball of radius $R_{inner} = 0.99R$ that repels all mesh points with a steep repulsive potential. The repulsive potential prevents vertices from moving closer than a small amount to the center of the sphere, thus arresting the oscillatory buckling mode. The mesh is colored by the distance of each point from the centre in units of R, to highlight small differences. Note the periodic array of indentations with amplitudes that vary slowly over the surface.

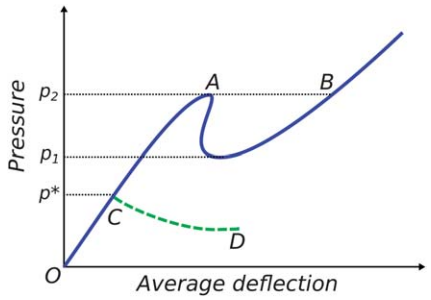

Fig. 4 Representative pressure–deflection curve for a clamped shallow spherical cap (after ref. 22). The deflection is averaged over the area of the cap (see eqn (35)). Upon increasing the pressure, the average deflection jumps from A to B at the pressure p_2. The green dashed curve CD that branches off at p^* corresponds to a nonaxisymmetric deformation.

the external pressure by either deforming continuously or by snap-through buckling when a threshold pressure is reached. The influence of the cap on the remainder is only expected to extend over a narrow region of width ℓ into the area occupied by the remainder. As a result, we expect the equations of shallow shell theory to also accurately describe the stresses in the remainder for small soft caps. We use polar coordinates, locating the origin at the center of the cap. We then have two sets of equations, one for the cap (with fields $\tilde{W}$, $\tilde{\chi}$ and elastic moduli $\tilde{Y}$, $\tilde{\kappa}$) when $r < R\alpha$ and one for the remainder (with fields W, χ and elastic moduli Y, κ) when $r > R\alpha$. The fields are related by matching displacements, stresses and moments at the boundary, $r = R\alpha$.

A Mechanism for snap-through buckling

In the limit of an infinitely stiff remainder ($\tau = \tilde{h}/h \to 0$), all displacements along the cap boundary are restricted, and by continuity of slopes the slope of the cap shape at the boundary is fixed to be α. This limit corresponds to the problem of buckling of an elastic cap, clamped along the entire edge to restrict all deformations, under hydrostatic pressure. The buckling of clamped caps is a well-studied problem in shell theory, with a definitive numerical analysis conducted by Huang.[22] We expect that the snap-through buckling of caps embedded in thin shells with a stiff remainder follows a similar mechanism, which we summarize here.

At each value of pressure, one or more equilibrium solutions may exist for the fields within the cap. The signature of loss of stability under pressure is seen in the pressure–deflection curve associated with these solutions, qualitatively illustrated in Fig. 4 (after ref. 22). The curve OAB in Fig. 4 shows a representative pressure–deflection relation for axisymmetric deflections. At low enough pressures, an analysis of the linearized equations shows that the cap deforms axisymmetrically and the deflection averaged over the cap,

$$\overline{\tilde{W}} = \frac{\int_0^{r_0} r\tilde{W}(r)\mathrm{d}r}{\int_0^{r_0} r\mathrm{d}r}, \tag{35}$$

grows with pressure ($r_0 = R\alpha$ is the radius of the soft spot boundary). At higher pressures, however, nonlinear effects become important, and the governing equations of the cap admit multiple solutions that satisfy the boundary conditions. In the range $p_1 < p < p_2$, for instance, three solutions exist at each pressure. When this happens, the pressure–deflection relation is no longer single-valued. With increasing pressure, at the maximum point A where two of the solutions merge, the cap deflection jumps directly to point B, signifying axisymmetric snap-though at pressure p_2. A subsequent slow decrease in pressure leads to a "snap-back" in the shape at the pressure p_1. We study this mechanism for caps embedded in spherical shells in Section VI E.

However, for caps beyond a certain size, a *non*-axisymmetric deflection mode may appear at a lower pressure p^*, with as a pressure–deflection relation of the form of the dashed line in Fig. 4. Unlike the axisymmetric mode, the nonaxisymmetric deflection modes are highly degenerate. A stability analysis of such modes in shallow shells[2] shows that there is no stable shape in the vicinity of such a state; *i.e.* the slope of the curve CD is indeed negative at C. Therefore, the appearance of a nonaxisymmetric mode at $p^* < p_2$ triggers snap-through buckling of the cap to an inverted shape *via* the path OCD. In Fig. 4, we show $p^* < p_1$ for clarity, although this inequality need not hold in general. We consider the nonaxisymmetric buckling mode for our caps in Section VI D. In our analysis, we assume that the appearance of a nonaxisymmetric deflection in the cap immediately triggers snap-through buckling of the cap, which is the case for clamped caps.[22]

B Non-dimensionalizing the equations

Since the snap-through of the cap is primarily determined by the deflections and stresses in the cap itself, we rescale all quantities with physical parameters that depend on the elastic properties of the cap. We define the nondimensional radial coordinate and pressure:

$$s = \frac{r}{\tilde{\ell}}, \tag{36}$$

$$\eta = \frac{p}{\tilde{p}_0} = \frac{pR^2}{4\sqrt{\tilde{\kappa}\tilde{Y}}}, \tag{37}$$

where $\tilde{\ell} = R/\tilde{\gamma}^{1/4}$ and $\tilde{p}_0 \equiv 4\sqrt{\tilde{\kappa}\tilde{Y}}/R^2$ is the classical buckling pressure associated with a uniform spherical shell with the elastic properties of the cap. We also define the rescaled fields in both the cap and the remainder

$$\tilde{w} = \frac{R}{\tilde{\ell}^2}\tilde{W}, \quad \tilde{\phi} = \frac{R^2}{\tilde{Y}\tilde{\ell}^4}\tilde{\chi}; \tag{38}$$

$$w = \frac{R}{\tilde{\ell}^2}W, \quad \phi = \frac{R^2}{\tilde{Y}\tilde{\ell}^4}\chi. \tag{39}$$

Upon substituting these quantities into the shell equations [eqn (18) and (20)], we obtain the following nondimensional equations for the cap:

$$\nabla^4\tilde{w} - \nabla^2\tilde{\phi} - N_2(\tilde{\phi},\tilde{w}) = 4\eta, \tag{40}$$

$$\nabla^4\tilde{\phi} + \nabla^2\tilde{w} + \frac{1}{2}N_2\left(\tilde{w},\tilde{w}\right) = 0, \tag{41}$$

and for the remainder:

$$\frac{1}{\tau^3}\nabla^4 w - \nabla^2\phi - N_2(\phi, w) = 4\eta, \tag{42}$$

$$\tau\nabla^4\phi + \nabla^2 w + \frac{1}{2}N_2(w, w) = 0, \tag{43}$$

where the differential operators are now defined using the variables (s,θ) rather than (r,θ).

From this analysis, we see that when cap size is rescaled by the elastic length scale $\tilde{\ell}$ and pressure by the classical buckling pressure $\tilde{p}_0$, the dependence on elastic moduli drops out, and caps of vastly different properties but the same thickness ratio τ relative to the remainder of the shell can be described by just two dimensionless quantities $\tilde{\lambda} = R\alpha/\tilde{\ell}$ and $\eta = p/\tilde{p}_0$ (as long as they are small enough that shallow shell theory applies).

Fig. 5 plots the pressure of the *first* buckling transition $\eta_{c_1} = p_{c_1}/\tilde{p}_0$ (whether it corresponds to a snap-through transition of the cap as for $\tau < 0.5$, or a collapse of the whole shell as for $\tau > 0.5$), as a function of the parameters τ and $\tilde{\lambda}$. When compared to Fig. 2, we see that the buckling pressures, when rescaled using $\tilde{p}_0$, vary over a much smaller range and display similar behavior as τ is changed. This observation suggests that the first buckling transition of the shell is always a snap-through transition of the cap, and that the mechanism of the snap-through does not vary significantly as τ is changed. Indeed, all of the η_{c_1} *vs.* $\tilde{\lambda}$ curves for the buckling pressure share similar characteristics for the dependence of buckling pressure on cap size: there is an apparent kink in the range $5 < \tilde{\lambda} < 6$ that separates a convex dependence for smaller caps from a roughly constant dependence for larger caps. A similar feature is seen in the buckling pressure curve for *clamped* caps, *i.e.* shallow sections of spheres with clamped circular edges under pressure.[22] In that case, the kink separates values of $\tilde{\lambda}$ for which the buckling mode is *axisymmetric i.e.* with no circumferential angular dependence

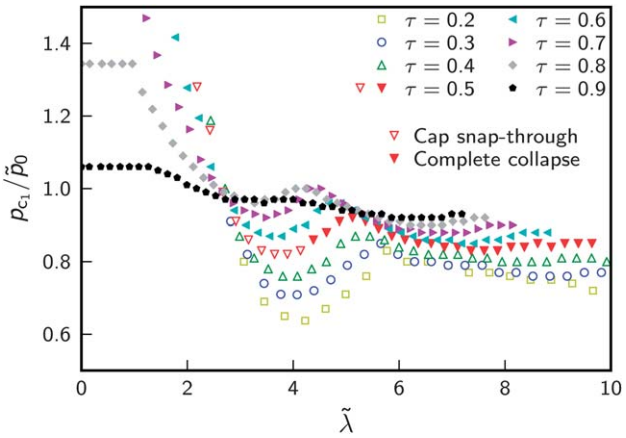

Fig. 5 Reduced pressure $p_{c_1}/\tilde{p}_0$ of the first buckling event, whether a snap-through of the cap (for shells following buckling pathway I, empty symbols), or a catastrophic collapse of the whole shell (buckling pathways II and III, filled symbols), as a function of the dimensionless spot size $\tilde{\lambda} = \alpha\tilde{\gamma}^{1/4}$ in buckling simulations on shells with $\gamma = 10^4$. The data shown is the same as for the first buckling event in Fig. 2, but is rescaled using the cap parameters $\tilde{p}_0$ and $\tilde{\lambda}$ rather than the shell parameters p_0 and λ.

about the z axis, from $\tilde{\lambda}$ values for which the buckling is nonaxisymmetric and has some circumferential variation. Furthermore, no snap-through buckling is observed for clamped caps with $\tilde{\lambda} < 3.3$; below this size the cap deforms continuously as the pressure is increased. This is similar to the present case with shells that follow buckling pathway III, where no snap-through buckling of the cap is observed.

We first use our numerical results to test whether the structure of the η_{c_1} *vs.* $\tilde{\lambda}$ curves is linked to the buckling mode. We investigate the nature of the buckling mode that drives the snap-through of the cap by arresting its growth with an internal repulsive potential, as was done for the uniform sphere in Section V. Fig. 6 illustrates the buckling mode that drives snap-through of the cap, as the cap size is varied for a shell with $\gamma = 10^4$ and $\tau = 0.4$. For small caps, the buckling mode is axisymmetric, whereas for large caps, it has a periodic structure in the circumferential direction, similar to the situation for clamped caps.[22] The nature of the buckling mode changes from axisymmetric to nonaxisymmetric around $\tilde{\lambda} = 5$, which corresponds to the kink in the η_{c_1} *vs.* $\tilde{\lambda}$ curve for $\tau = 0.4$ (see Fig. 5). The number of nodes in the circumferential direction then increases with cap size, although the wavelength of the buckling mode itself is hardly changed from an intrinsic size of order $\tilde{\ell}$. The dependence of the buckling pressure on cap size $\tilde{\lambda}$ in the nonaxisymmetric region is also weak.

This structure is retained for other values of τ, although the $\tilde{\lambda}$-value of the transition from axisymmetric to nonaxisymmetric buckling falls as τ approaches the uniform shell limit, $\tau = 1$. The roughly constant value of η_{c_1} for nonaxisymmetric buckling also approaches 1 as $\tau \to 1$, which is expected because buckling of a uniform shell with the thickness of the cap would happen at $\eta = 1$.

C Analysis of linearized equations

The buckling of the cap is a nonlinear phenomenon, that arises due to the coupling terms in the shell equations [eqn (40)–(43)],

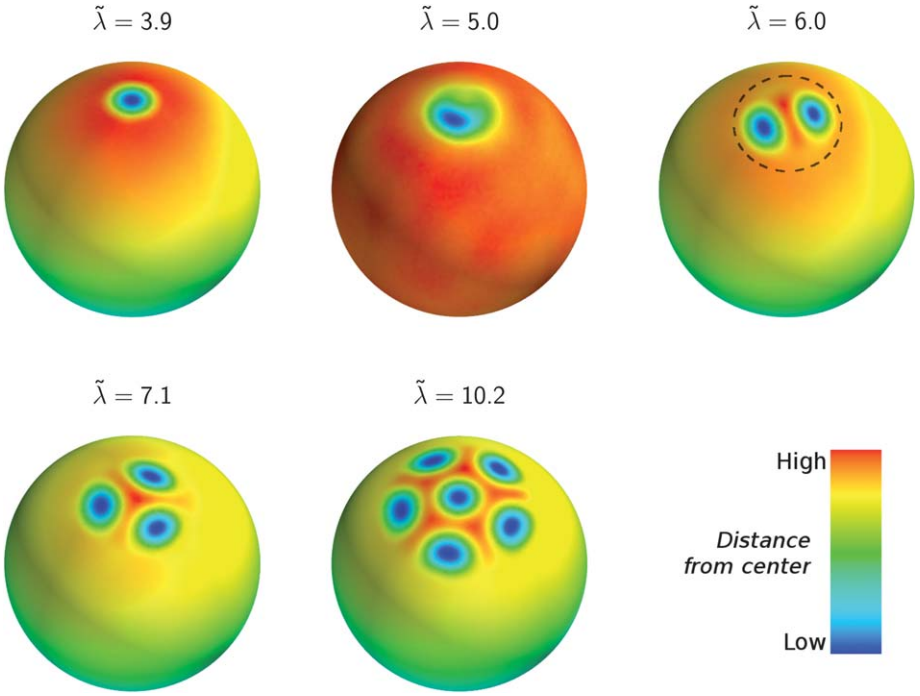

Fig. 6 (a) Mode for snap-through buckling of a soft cap, for shells with $\gamma = 10^4$, $\tau = 0.4$, and various dimensionless cap sizes $\tilde{\lambda} = \alpha\tilde{\gamma}^{1/4}$. The buckling mode was arrested in numerical simulations by including an inner ball of radius $R_{\text{inner}} = 0.99R$ whose surface repels all mesh points with a steep repulsive potential. The mesh is colored by the distance of each point from the center of the sphere on a linear color scale, to highlight small differences. The soft region coincides with the region of large variations in deflection at the top of each shell—as an illustration, the dashed line shows the boundary of the soft region for the shell with $\tilde{\lambda} = 6.0$.

which puts an exact analytical study out of reach. However, we can gain some insight about the behavior under pressure and the approach to buckling by linearizing the equations about some appropriate state of stress to get the so-called *Reissner* equations of shallow-shell theory.[30,31] We saw in Section V that a uniform shell contracts uniformly up to the point of buckling; we can expand deflections and stresses about this state of uniform pre-stress.

In the cap, the rescaled uniform radial deflection $\tilde{w}_0 = 2\eta(1 - \nu)$ and Airy function $\tilde{\phi}_0 = -s^2\eta$ solve the shell equations exactly. Upon substituting $\tilde{w} = \tilde{w}_0 + \tilde{w}_1$ and $\tilde{\phi} = \tilde{\phi}_0 + \tilde{\phi}_1$ in eqn (40) and (41) and keeping terms linear in $\tilde{w}_1$ and $\tilde{\phi}_1$, we get the Reissner equations within the cap:

$$\nabla^4\tilde{w}_1 + 2\eta\nabla^2\tilde{w}_1 - \nabla^2\tilde{\phi}_1 = 0, \tag{44}$$

$$\nabla^4\tilde{\phi}_1 + \nabla^2\tilde{w}_1 = 0. \tag{45}$$

General axisymmetric solutions to the differential equations that satisfy the requirement of continuous and finite stresses at the origin are written in terms of real and imaginary parts of J_0, the Bessel function of the first kind:

$$\tilde{w}_1(s) = c_1\left[J_{\mathrm{R}}(s) + \frac{\eta}{\sqrt{1-\eta^2}}J_{\mathrm{I}}(s)\right] + c_2\left[J_{\mathrm{I}}(s) - \frac{\eta}{\sqrt{1-\eta^2}}J_{\mathrm{R}}(s)\right] + c_3, \tag{46}$$

$$\tilde{\phi}_1(s) = \frac{1}{\sqrt{1-\eta^2}}[c_1 J_{\mathrm{I}}(s) - c_2 J_{\mathrm{R}}(s)], \tag{47}$$

where

$$J_{\mathrm{R}}(s) \equiv \mathrm{Re}\left[J_0(\tilde{\rho}s)\right];\ J_{\mathrm{I}}(s) \equiv \mathrm{Im}\left[J_0(\tilde{\rho}s)\right];\ \tilde{\rho} \equiv \left(\eta + i\sqrt{1-\eta^2}\right)^{1/2}. \tag{48}$$

Similarly, substituting $w = w_0 + w_1$ and $\phi = \phi_0 + \phi_1$, where $w_0 = 2\eta(1 - \nu)\tau$ and $\phi_0 = -s^2\eta$, into the nonlinear equations for the remainder (eqn (42) and (43)), and keeping terms linear in w_1 and ϕ_1, gives the Reissner equations for the remainder:

$$\frac{1}{\tau^3}\nabla^4 w_1 + 2\eta\nabla^2 w_1 - \nabla^2\phi_1 = 0, \tag{49}$$

$$\tau\nabla^4\phi_1 + \nabla^2 w_1 = 0. \tag{50}$$

In the remainder, we look for solutions to the deflection and stress that decay to zero as $s \to 0$. These can be written in terms of $H_0^{(1)}$, the Hankel function of the first kind:

$$w_1(s) = c_4\left[H_{\mathrm{R}}(s) + \frac{\eta\tau^2}{\sqrt{1-\eta^2\tau^4}}H_{\mathrm{I}}(s)\right] + c_5\left[H_{\mathrm{I}}(s) - \frac{\eta\tau^2}{\sqrt{1-\eta^2\tau^4}}H_{\mathrm{R}}(s)\right], \tag{51}$$

$$\phi_1(s) = \frac{1}{\tau^2\sqrt{1-\eta^2\tau^4}}[c_4 H_{\mathrm{I}}(s) - c_5 H_{\mathrm{R}}(s)], \tag{52}$$

where

$$H_R(s) \equiv \mathrm{Re}\left[H_0^{(1)}(\rho s)\right];\ H_I(s) \equiv \mathrm{Im}\left[H_0^{(1)}(\rho s)\right];$$
$$\rho \equiv \left(\tau^3\eta + i\tau\sqrt{1-\eta^2\tau^4}\right)^{1/2}. \quad (53)$$

At the boundary we require continuity of the transverse deflection W and its first derivative $W_{,r}$, the radial displacement $U = r(u_{\theta\theta} + W/R)$ [or equivalently the strain component $u_{\theta\theta} = (\chi_{,rr} - \nu\chi_{,r}/r)/Y$], the radial stress $\sigma_{rr} = \chi_{,r}/r$, and the bending moment $M_{rr} = -\kappa(W_{,rr} + \nu W_{,r}/r)$. The resulting dimensionless equations, to be satisfied at the cap edge $s = \tilde{\lambda}$, are:

$$\tilde{w} = w,\ \tilde{w}_{,s} = w_{,s},\ \tilde{\phi}_{,s} = \phi_{,s}; \quad (54)$$

$$\tilde{\phi}_{,ss} - \nu\frac{\tilde{\phi}_{,s}}{\tilde{\lambda}} = \tau\left(\phi_{,ss} - \nu\frac{\phi_{,s}}{\tilde{\lambda}}\right); \quad (55)$$

$$\tau^3\left(\tilde{w}_{,ss} + \nu\frac{\tilde{w}_{,s}}{\tilde{\lambda}}\right) = \left(w_{,ss} + \nu\frac{w_{,s}}{\tilde{\lambda}}\right). \quad (56)$$

Note that the non-constant components $\tilde{w}_1$, w_1, $\tilde{\phi}_1$, ϕ_1 must be nonzero for $\eta > 0$ since $\tilde{w}_0 \neq w_0$, $\tilde{\phi}_{0,s} \neq \phi_{0,s}$. For each pair of $\{\eta,\tilde{\lambda}\}$ values, the boundary conditions give rise to five linear equations which can be solved for the five constants $c_1 \ldots c_5$. We will call the result the *Reissner solution* for the deflection and stresses in the cap and the remainder.

Fig. 7 compares the solution of the Reissner equations to the transverse deflection from simulations for a few shells, with η values below the buckling threshold. The linearized solutions capture many features of the full solution, particularly in the vicinity of the boundary between the cap and the remainder and the period of the decaying oscillations in the cap.

D Nonaxisymmetric buckling

The solution of the linearized equations is sufficient to obtain a qualitative understanding of the nonaxisymmetric buckling of large caps, which we have seen is largely independent of the cap size $\tilde{\lambda}$ for each value of τ. Fig. 8 shows the behavior of the axisymmetric Reissner solution for $\eta = 0.8$, close to the snap-through pressure, for caps of various sizes and thickness ratios relative to the remainder. This is expected to approximate the axisymmetric deflection of the shell before the non-axisymmetric mode appears and causes the cap to snap through. From Fig. 8(a), we see that the solution develops a boundary layer which does not change significantly when $\tilde{\lambda} > 10$; the solutions for large cap size are related to each other by a simple shift along the r axis. (Clamped caps display a similar behavior.[22]) Since the stresses are also largest in this region close to the cap–shell boundary, the behavior here dominates the buckling transition. It is likely that the relative insensitivity of the buckling pressure to the cap size for large caps is a consequence of boundary layer dominance.

To quantify this effect, we estimate the coupling between the excess stresses due to the boundary and any nonaxisymmetric mode that may arise. Recall that for uniform shells, the nontrivial buckling mode arose due to the coupling between gradients of the transverse displacement W_1 and the uniform pre-stress $\sigma_{xx} = \sigma_{yy} = -pR/2$ (Section V). Now we have an axisymmetric pre-stress $\{\tilde{w}_a,\tilde{\phi}_a\}$ that varies in the r direction, which couples to nonaxisymmetric fields $\{\tilde{w}_n,\tilde{\phi}_n\}$ which we shall assume small. We substitute $\tilde{w} = \tilde{w}_a + \tilde{w}_n$ and $\tilde{\phi} = \tilde{\phi}_a + \tilde{\phi}_n$ into the full nonlinear shell equations [eqn (40) and (41)] and keep terms linear in the nonaxisymmetric fields. For simplicity, we work in scaled Cartesian coordinates at a position on the x axis near the cap–shell boundary, so that $\tilde{w}_a(s) \approx \tilde{w}_a(x)$, and $x \approx \tilde{\lambda} \gg 1$ which means that the θ direction coincides approximately with the y direction. Then the nonlinear coupling gives rise to terms of the form $\tilde{w}_{a,xx}\tilde{\phi}_{n,yy}$, $\tilde{\phi}_{a,xx}\tilde{w}_{a,yy}$ and $\tilde{w}_{a,xx}\tilde{w}_{n,yy}$. The equations for $\tilde{w}_n$ and $\tilde{\phi}_n$ now read

$$\nabla^4\tilde{w}_n - \nabla^2\tilde{\phi}_n - \tilde{w}_{a,xx}\tilde{\phi}_{n,yy} - \tilde{\phi}_{a,xx}\tilde{w}_{a,yy} = 0, \quad (57)$$

$$\nabla^4\tilde{\phi}_n + \nabla^2\tilde{w}_n + \tilde{w}_{a,xx}\tilde{w}_{n,yy} = 0. \quad (58)$$

For the uniform shell, only $\tilde{\phi}_{a,xx} = -2\eta$ was nonzero, but the presence of the cap–remainder boundary gives rise to a spatially varying $\tilde{w}_n$ and thus a nonzero $\tilde{w}_{a,xx}$ as well. In fact, $\tilde{\phi}_{a,xx} \approx -2\eta$ remains a good approximation to the pre-buckling Airy stress function in the cap, so the additional effects which bring down

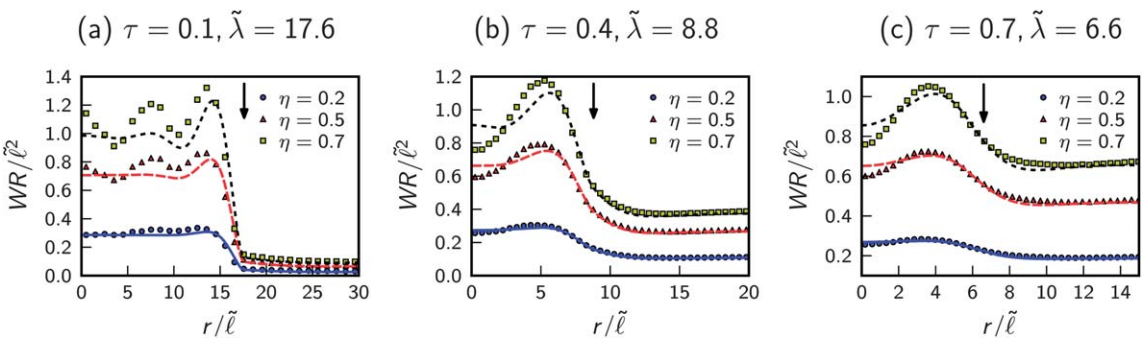

Fig. 7 Comparison of the scaled normal deflection $WR/\tilde{\ell}^2$ as a function of radial position $r/\tilde{\ell}$ measured from simulations with an amorphous mesh (symbols), to the solution of the linearized shell equations (lines), for different values of the reduced pressure η. The values from simulations are obtained by averaging the positions of all mesh points sharing each r value (*i.e.* over all values of θ for each value of r). The three subfigures (a–c) correspond to three different shells, all with $\gamma = 10^4$ and cap angle $\alpha = \cos^{-1}(0.85)$, but with different cap-to-shell thickness ratios τ which changes the elastic length $\tilde{\ell}$ and therefore the dimensionless cap size $\tilde{\lambda} = R\alpha/\tilde{\ell}$. The vertical arrows indicate the r position of the boundary between the soft cap and the remainder. All three shells buckle around $\eta = 0.8$.

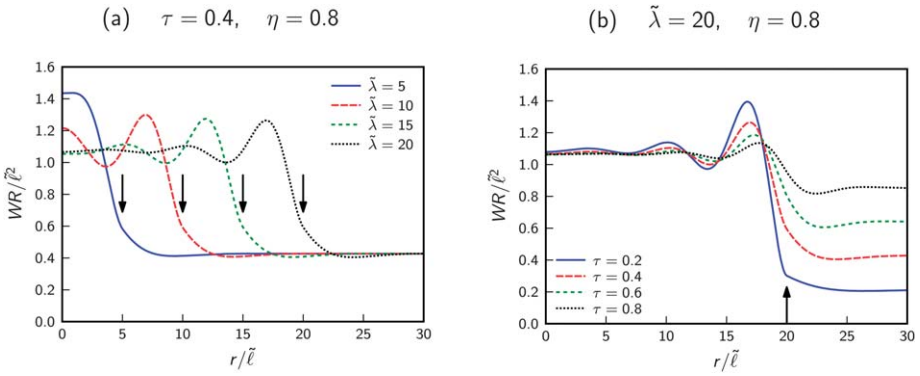

Fig. 8 Reissner solution for the scaled normal deflection $WR/\tilde{\ell}^2$ for caps with (a) increasing cap size $\tilde{\lambda}$ at constant pressure η and thickness ratio τ, and (b) increasing thickness ratio at constant pressure and cap size. The vertical arrows indicate the r position of the boundary between the soft cap and the remainder.

the buckling pressure below $\eta = 1$ are mainly due to the new coupling with $\tilde{w}_{a,xx}$. Let ξ denote a typical value of $\tilde{w}_{a,xx}$ in the boundary layer region. A rough estimate of its effect can be obtained from the equations

$$\nabla^4 \tilde{w}_n - \nabla^2 \tilde{\phi}_n - \xi \tilde{\phi}_{n,yy} + 2\eta \tilde{w}_{a,yy} = 0, \tag{59}$$

$$\nabla^4 \tilde{\phi}_n + \nabla^2 \tilde{w}_n + \xi \tilde{w}_{n,yy} = 0. \tag{60}$$

Similar in spirit to the stability calculation for uniform shallow shells, we look for solutions that oscillate in the y direction of the form $\tilde{w}_n, \tilde{\phi}_n \propto e^{iqy}$, which leads to the eigenvalue equation

$$q^4 - 2\eta q^2 + (1 + \xi)^2 = 0. \tag{61}$$

Therefore, oscillatory solutions with $q^2 > 0$ exist only if

$$\eta > 1 + \xi. \tag{62}$$

According to this argument, regions of the axisymmetric deflection with negative curvature in the radial direction, $\xi \sim \tilde{w}_{a,ss} < 0$, cause nonaxisymmetric modes to appear at $\eta \approx 1 + \xi < 1$. The Reissner solution, as well as the full nonlinear solution, display these regions prominently in the boundary region near the cap–shell boundary (see Fig. 7 and 8). Therefore, the coupling of the nonaxisymmetric deformation with the pre-buckling axisymmetric solution can in fact give rise to a nonaxisymmetric solution at pressures *below* $\tilde{p}_0$, the buckling pressure of a complete shell with the same properties as the cap.

Fig. 7 and 8 show that the most negative value of the curvature in the axisymmetric deflection, $\tilde{w}_{a,xx}$, occurs at the sharp peak in $\tilde{w}_a$ in the boundary layer. The magnitude of the curvature depends on the pressure as well as the cap–shell thickness ratio. To estimate when a nonaxisymmetric mode may first arise, we take the value of $\tilde{w}_{a,xx}$ at this peak to be the scale ξ. We use the Reissner solution to find $\xi(\eta)$; the value $\eta_{Reissner}$ that solves the self-consistent equation $\eta = 1 + \xi(\eta)$ is a rough estimate of the buckling pressure. Fig. 9 shows the result for large caps with different values of τ. Although our estimate ignores the s-dependence of $\tilde{w}_{a,xx}$ and the boundary conditions on $\tilde{w}_{a,xx}$ and $\tilde{w}_n$, it successfully reproduces the features associated with the nonaxisymmetric buckling pressure: $\eta_{Reissner}$ approaches an approximately constant value for $\tilde{\lambda} \gtrsim 6$, and this value gets closer to 1 as $\tau \to 1$.

Our rough calculation also predicts the inverse wavelength of the circumferential buckling mode. The solution to eqn (61) at the buckling pressure $\eta = 1 + \xi$ is $q = \sqrt{1 + \xi} = \sqrt{\eta}$. Thus, the length scale of the circumferential oscillation is expected to be unchanged in the nonaxisymmetric buckling region, in agreement with Fig. 6.

E Axisymmetric buckling

In the small $\tilde{\lambda}$ region, to the left of the kink in the buckling pressure curves (Fig. 5), we have seen that the snap-through is axisymmetric. The axisymmetric Reissner solution to the linearized equations, eqn (44), (45), (49), and (50), shows no discontinuity in the deflection as the pressure is increased; thus, the discontinuous snap-through of the cap happens only when the nonlinear terms are significant in the governing equations of the cap. To simplify our analysis, we assume that deflections in the remainder are small, so that the linearized approach

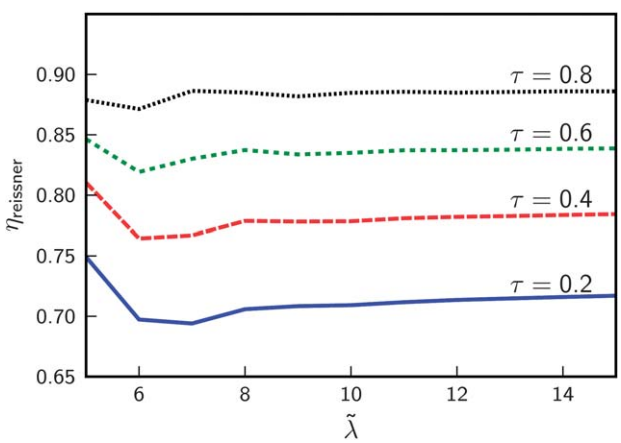

Fig. 9 Estimate of the reduced pressure $\eta = p/\tilde{p}_0$ at which a nonaxisymmetric mode arises in the cap for various thickness ratios, using the criterion of eqn (62) with the largest value of second derivative $\tilde{w}_{a,xx}$ of the Reissner solution for the cap as the estimate for ξ.

introduced in Section VI C still applies in the remainder and the Reissner solution is sufficient to describe its response. This approximation is accurate for small thickness ratios τ, when the snap-through of the cap happens at small pressures compared to the buckling pressure of the remainder (Fig. 2).

In the axisymmetric region, $\tilde{w}$ and $\tilde{\phi}$ are functions solely of s and the nonlinear governing equations of the cap [eqn (40) and (41)] simplify to

$$\nabla^4\tilde{w} - \nabla^2\tilde{\phi} - \frac{1}{s}\left(\tilde{\phi}_{,s}\tilde{w}_{,ss} + \tilde{w}_{,s}\tilde{\phi}_{,ss}\right) = 4\eta, \tag{63}$$

$$\nabla^4\tilde{\phi} + \nabla^2\tilde{w} + \frac{1}{s}\tilde{w}_{,s}\tilde{w}_{,ss} = 0, \tag{64}$$

expressions which can be integrated once to give equations for the derivative functions $\Theta \equiv -\tilde{w}_{,s}$ and $\Phi \equiv \tilde{\phi}_{,s}$:[22,32]

$$s\Theta_{,ss} + \Theta_{,s} - \frac{\Theta}{s} + s\Phi - \Theta\Phi + 2\eta s^2 = 0, \tag{65}$$

$$s\Phi_{,ss} + \Phi_{,s} - \frac{\Phi}{s} - s\Theta + \frac{\Theta^2}{2} = 0. \tag{66}$$

In addition to these equations and the linearized equations [eqn (49) and (50)] in the remainder, the continuity equations [eqn (54)–(56)] must be satisfied at the boundary between cap and remainder.

1 Qualitative analysis. An approximate analytical solution to the nonlinear equations, computed using the Galerkin method[33] recovers many aspects of the snap-through buckling transition. We first consider the previously studied clamped cap limit,[22] which corresponds to an infinitely stiff remainder, *i.e.* $\tau \to 0$. For a clamped cap, the tangent slope and all deformations at the boundary are fixed, whereas the shape and stresses at the origin must be continuous, which leads to the following boundary conditions for Θ and Φ:

$$\Theta(0) = \Phi(0) = 0, \tag{67}$$

$$\Theta(\tilde{\lambda}) = 0, \tag{68}$$

$$\tilde{\lambda}\Phi_{,s}(\tilde{\lambda}) - \nu\Phi(\tilde{\lambda}) = 0. \tag{69}$$

For small caps that exhibit axisymmetric buckling ($\tilde{\lambda} \lesssim 5$), the size of the cap is smaller than the length scale of oscillatory variations in $\tilde{w}$, which is set by $\tilde{\ell}$. As a result, the inward deflection $\tilde{w}$ has a maximum at the centre of the cap and decays monotonically to zero at the cap boundary. Correspondingly, $\Theta(s)$ is zero at the origin and the cap boundary, and has a single extremal point in between. Many characteristics of the full solution to the nonlinear equations can be obtained by considering an approximate solution which reproduces these main features. We choose as our trial solution

$$\Theta(s) = As\left(1 - \frac{s}{\tilde{\lambda}}\right), \tag{70}$$

which automatically satisfies the boundary conditions. We obtain the value of A that best approximates the true solution using the Galerkin procedure: the trial solution, substituted into eqn (66), provides a linear differential equation for Φ which can be solved with the corresponding boundary conditions to obtain a trial solution for $\Phi(s)$ that also depends on A. These solutions are substituted into the left hand side of eqn (65), which is then multiplied by $\Theta(s)\mathrm{d}s$ and integrated from $s = 0$ to $s = \lambda$ to get a third order algebraic equation for the deflection amplitude A:

$$\tilde{\lambda}^4(194A^3 - 1581A^2 + 2952A) + 151\,200A - 60\,480\tilde{\lambda}^2\eta = 0. \tag{71}$$

Roots of this equation provide the best estimate of the solution for the cap shape at any pressure. The buckling mechanism is evident from the nature of these roots. For small values of $\tilde{\lambda}$, eqn (71) has a single real solution for all values of the pressure, and the average deflection increases continuously as a function of η. This corresponds to buckling pathway III for small caps, in which the cap deforms smoothly to its inverted shape without snapping. However, for $\tilde{\lambda} > 3.25$, there is a range of pressures for which A, and consequently the cap-averaged deflection $\overline{\tilde{\omega}}$, can take on three real values. As a result, the pressure–deflection curves, shown in Fig. 10(a), take on the characteristic form of curve *OAB* in Fig. 4, and snap-through buckling occurs at the maximal value of η at which three real solutions exist (*i.e.*, at point *A* in Fig. 4). This snap-through pressure is obtained in the Galerkin solution by setting the discriminant of eqn (71) to zero, and the solution is shown as the bottom curve in Fig. 10(b). The approximate solution reproduces many features of the buckling pressure of clamped caps in the axisymmetric region, such as the absence of a snap-through for caps below a certain size, and a non-monotonic dependence of buckling pressure on cap size.

Embedding the cap in a more flexible shell requires modifying the boundary conditions from the clamped limit. The full effect of the remainder on the cap at the boundary is complicated, and cannot be expressed succinctly. Requiring continuity of stresses and deformations across the boundary replaces eqn (68) and (69) with equations that relate the displacement and rotation angle at the boundary to the corresponding stresses and bending moments, themselves implicitly dependent on the solution to Θ and Φ. However, the qualitative effect of the remainder on the boundary conditions can be gauged from the Reissner solutions, which satisfy the same continuity conditions, albeit for linearized versions of the governing equations. The Reissner solutions suggest that as τ is changed from zero, $\Theta(\tilde{\lambda})$ will be positive but remains small, whereas $\Phi_{,s}(\tilde{\lambda}) - \nu\Phi(\tilde{\lambda})/\tilde{\lambda}$, which is proportional to the circumferential strain $u_{\theta\theta}$, will be negative because of the compression of the remainder under external pressure. As the thicknesses in the cap and the remainder become comparable, this circumferential strain becomes larger in magnitude. The qualitative effect of this modified boundary condition on our approximate solution can be assessed by replacing the boundary condition on Φ, eqn (69), with

$$\tilde{\lambda}\Phi_{,s}(\tilde{\lambda}) - \nu\Phi(\tilde{\lambda}) = \varepsilon, \tag{72}$$

where $\varepsilon < 0$ becomes increasingly negative as $\tau \to 1$, and recomputing the approximate Galerkin solution. The Reissner solutions show that $|\varepsilon|$ increases over a range $0 \lesssim |\varepsilon| \lesssim 2$ as τ is

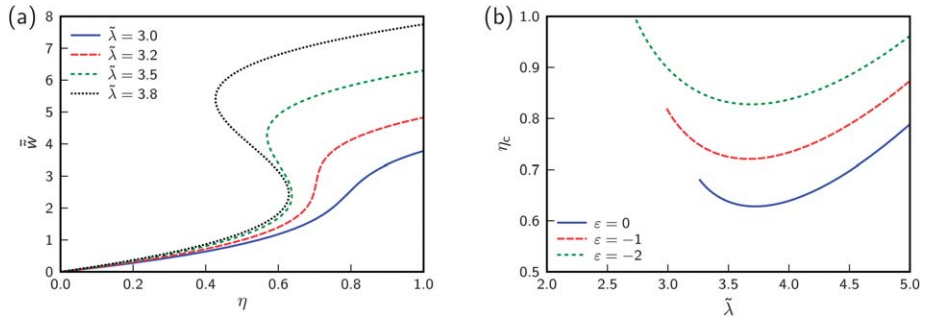

Fig. 10 (a) Deflection $\bar{\tilde{w}}$, averaged over the entire cap, as a function of the reduced pressure η, for the approximate solutions for the clamped cap obtained using the Galerkin method for different values of the cap size, $\tilde{\lambda}$. (b) Estimate of the buckling pressure using the Galerkin method, for different values of the circumferential strain ε at the boundary. The clamped cap corresponds to $\varepsilon = 0$.

increased from 0 to 1, for pressures in the range of 0.7–0.8. The variation in the corresponding estimate for the snap-through pressure is shown in Fig. 10(b). As the circumferential strain at the boundary increases, the snap-through buckling pressure curve moves upward and the smallest value of $\tilde{\lambda}$ at which buckling is observed decreases, both in qualitative agreement with the trends in the snap-through pressure as τ is increased (see Fig. 5). Although our analysis is a highly simplified description of the true boundary conditions (which in reality depend subtly on $\tilde{\lambda}$, τ and η), it qualitatively captures the effect of the remainder on the snap-through transition.

2 Numerical analysis of governing equations. To make our analysis more quantitative, we use the Reissner solution in the shell remainder to establish the boundary conditions on Θ and Φ at the boundary, and then numerically solve the nonlinear governing equations in the cap. The continuity conditions, eqn (54)–(56), together with eqn (49) and (50) for the fields in the remainder, can be reduced to two equations that must be satisfied by Θ, Φ and its derivatives at $s = \tilde{\lambda}$. These equations depend on the dimensionless quantities $\tilde{\lambda}$, η and τ. Together with eqn (67), they provide a complete set of boundary conditions for the nonlinear differential equations of the cap, eqn (65) and (66), which are then solved numerically using the bvp4c differential equation solver in the MATLAB (Mathworks Inc.) scientific computing package. A discontinuity in the pressure–deflection curve for the computed solutions signals the snap-through buckling pressure, which we compare to the snap-through buckling pressure from simulations in Fig. 11. The results quantitatively replicate the observed behavior in simulations at low values of τ. Deviations from the results of simulations become larger as τ increases, because our assumption of linear behavior in the remainder becomes less accurate as $\tau \to 1$. However, these results confirm that snap-through buckling of the cap happens *via* an axisymmetric mode for small values of τ, which arises due to nonlinear couplings between deformations and stresses in the cap. The remainder influences the boundary conditions on these deformation and stress fields, which shifts the snap-through pressure closer to $\eta = 1$ as $\tau \to 1$.

Our results show that the dependence of the first buckling pressure p_{c_1} on the spot size and thickness can be explained by

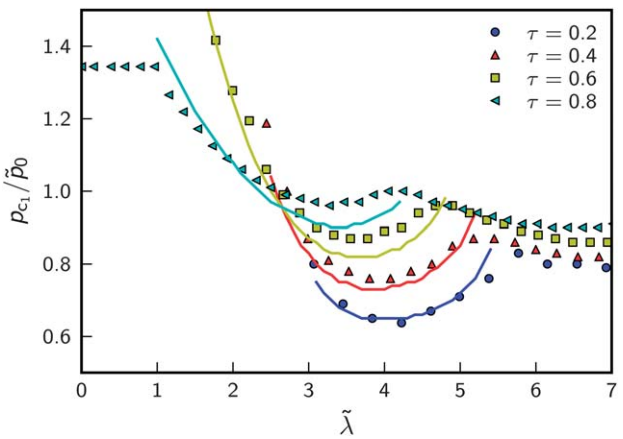

Fig. 11 Snap-through pressure estimate from numerically solving the governing equations of the cap with boundary conditions set by the Reissner solution for the remainder (solid lines), compared to p_{c_1}, the first buckling pressure measured in simulations (symbols).

the loss of stability of a spherical cap of dimensionless size $\tilde{\lambda}$, embedded in a remainder whose relative stiffness depends on the thickness ratio τ. Significantly, this "snap-through" loss of stability of the cap determines p_{c_1} for both buckling pathways I and II, even though the shapes of the shells at p_{c_1} differ dramatically between the two pathways (a snap-through localized to the cap for shells following pathway I, as opposed to a catastrophic collapse for shells following pathway II). From Fig. 2, we see that the transition from pathway I to pathway II occurs when this snap-through buckling pressure curve moves above the second buckling pressure p_{c_2} at which an inversion localized to the soft cap becomes unstable to catastrophic growth into the remainder of the shell. In contrast to p_{c_1}, which is determined primarily by the elastic properties of the cap, this second loss of stability is set mainly by the elastic properties of the remainder. We analyze this second loss of stability in the following section.

VII Collapse of the remainder

Whether through a continuous deformation or a snap-through buckling event, the soft cap attains an inverted shape, at a

particular pressure determined largely by the thickness ratio τ (the dependence on the cap size itself is weak for large caps). The inversion is an example of a nearly isometric shape, that preserves the metric everywhere except for a narrow region at its rim (whose width is approximately the elastic length within the cap, $\tilde{\ell}$). When this inversion has formed, the fate of the remainder of the shell depends on the stability of the inversion against further growth into the remainder. A scaling argument shows why such an inversion is unstable for large enough pressures: suppose the inversion has grown so that the rim is entirely within the remainder. Then, as outlined in Section V, there exists an inversion depth $d_{\max}(p) \sim (\kappa/pR^3)^2 R\sqrt{\gamma}$ that separates stable inversions from unstable ones. Inversions of depth $d > d_{\max}(p)$ can reduce their net energy by growing deeper, leaving the shell unstable to complete collapse. Conversely, there is a pressure $p_I(d) \sim (\kappa\gamma^{1/4}/R^3)\sqrt{R/d} \sim p_0\gamma^{-1/4}\sqrt{R/d}$ above which an inversion of depth d grows uncontrollably leading to collapse of the whole shell. But the inversion of the soft cap has the effect of 'seeding' an inversion with a depth $d_0/R \equiv 1 - \cos\alpha \approx \alpha^2/2 \approx \lambda^2/2\sqrt{\gamma}$ within the remainder (here, d_0 is the cap height, an alternative way of measuring the cap size). If the snap-though of the cap happens at $p_{c_1} < p_I(d_0)$, the seeded inversion is stable over the range of pressures $p_{c_1} < p < p_I(d_0)$, and a second collapse of the whole shell occurs only when the pressure increases to $p_{c_2} = p_I(d_0)$. This corresponds to pathway I as described in Section III. However, if the cap thickness is so high that snap-through happens at $p_{c_1} > p_I(d_0)$ (note that p_{c_1} is set by the cap elastic parameters while p_I is set by the remainder) then the inversion of the cap is immediately unstable to further growth into the remainder, and only a single collapse of the whole shell is observed at $p = p_{c_1}$. This scenario corresponds to pathway II for collapse of the shell. Thus, a consideration of the stability of inversions at different pressures qualitatively explains the transition from pathway I to pathway II as the thickness of the cap increases relative to the shell (Fig. 2).

This approximate description does not take into account the precise evolution of the inversion energy as the rim of the inversion grows out of the cap into the remainder. This transition is crucial in determining the true value of $p_I(d_0)$ and thus the pressure of collapse of the remainder. We study it in detail in the rest of this section.

A Energetics of a nearly isometric inversion in a shell with a soft cap

To numerically investigate the energetics of inversions centered at the north pole for shells with soft caps, we artificially create inversions by indenting the mesh with hard spheres that are the same radius as the shell itself. (We use spherical indenters to avoid the polygonal inversions that are associated with inversions created by point indenters.[34] In the present case, inversions are 'seeded' by the perfectly circular soft cap, and thus we are interested in inversions with perfectly circular rims.) To maintain equilibrium of forces, we prepare shells with two identical caps—one at the north pole and one at the south pole—and then squeeze the sphere between two indenters at each pole, although we report physical quantities (volume change and energy) for just one of the resulting inversions. The equilibrium configuration and corresponding elastic energy of the mesh are obtained by numerical minimization in the presence of the indenters. The depth of the inversion is varied by changing the distance between the indenting hard spheres. To prevent the shell from sliding out from between the indenters, we restrict a few mesh vertices in the vicinity of the poles to move only in the z direction.

Fig. 12 shows the elastic energy of inversions of depth d for shells with soft caps of various sizes [reported in terms of the cap height $d_0 = R(1 - \cos\alpha)$] at zero pressure, keeping the elastic properties of the shell and the cap unchanged. All energy curves can be divided into three distinct regions: $d \ll d_0$, when the inversion rim is localized within the soft cap; $d \gg d_0$, when the rim is localized in the remainder, and a transition region around $d \approx d_0$. This division is a direct consequence of the fact that the inversion rim is localized to a narrow region whose width is set by the elastic length scale which is small in both the cap and the remainder. As a result, the elastic energy approaches the Pogorelov scaling form[26] with the appropriate elastic constants in the small-d and large-d regions: $E_{el} \to c\tilde{\kappa}\tilde{\gamma}^{1/4}(d/R)^{3/2} = c\tau^{5/2}\kappa\gamma^{1/4}(d/R)^{3/2}$ for $h \ll h_0$ and $E_{el} \to c\kappa\gamma^{1/4}(d/R)^{3/2}$ for $d \gg d_0$. The best fit to the numerics is for $c = 19$, which is consistent with estimates from asymptotic analyses of the nonlinear shell equations governing the elastic energy of the inversion[26,35] and was also independently checked *via* indentation simulations on uniform shells. The volume change associated with the inversion, meanwhile, is well-approximated by that of a perfectly isometric inversion and does not depend strongly on the cap size (see inset to Fig. 12).

The stability of an inverted soft cap at finite pressure can now be studied by examining the behavior of the total energy $E_{tot}(d) = E_{el}(d) - p\Delta V(d)$ as the pressure is ramped up. Fig. 13(a)

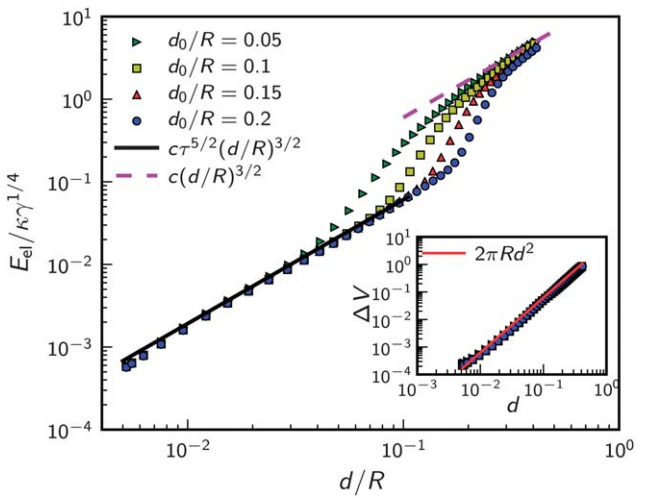

Fig. 12 Elastic energy associated with an inversion of depth d, at zero pressure, for a shell with a soft cap of height d_0. In all cases, $\gamma = 8000$ and $\tau = 0.4$. The lines correspond to the Pogorelov form of the elastic energy for a nearly isometric inversion localized in the cap (solid line) and remainder (dotted line) respectively, with dimensionless prefactor $c = 19$. *Inset*: the volume reduction ΔV associated with the inversion matches the expectation for a purely isometric inversion, $\Delta V_{iso} = 2\pi d^2(3R - d)/3 \approx 2\pi Rd^2$ for small caps.

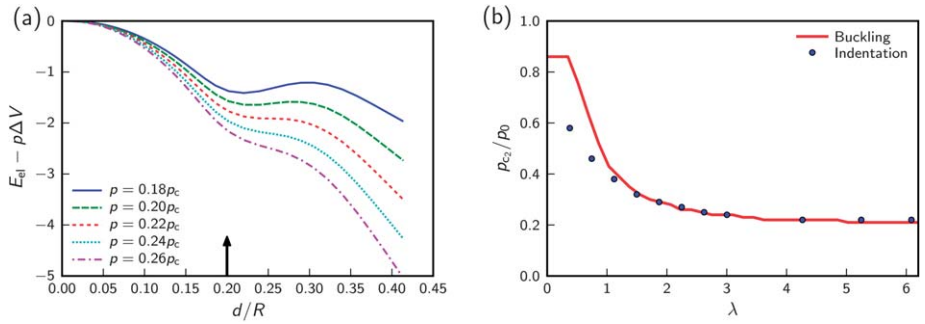

Fig. 13 (a) Total energy of an inversion in a pressurized shell with $\gamma = 8000$, $\tau = 0.4$ and $\lambda = 6.09$ (corresponding to a cap height $d_0 = 0.2R$), showing that the shell with inversion confined to the cap becomes unstable for $p > 0.22p_0$. The arrow indicates the r coordinate of the border between the cap and the remainder. (b) Collapse pressure estimated using stability considerations from indentation simulations (symbols) compared to p_{c_2}, the pressure of catastrophic collapse of the remainder measured from pressure buckling simulations (line) for shells with $\gamma = 8000$, $\tau = 0.4$, as a function of the dimensionless cap size λ.

shows the total elastic energy for a pressurized shell with $\gamma = 8000$, $\tau = 0.4$ and cap size $d_0 = 0.2R$ (corresponding to $\lambda \approx 6$). For this shell, the cap snaps through to an inverted shape at $p_{c_1} = 0.13p_0$. The inversion localized to the cap is stable for pressures up to $0.22p_0$ because of the existence of a local minimum in the energy curve at $d/R \approx 0.2$. However, at $p = 0.22p_0$, the energy minimum vanishes and the pressurized shell can reduce its energy indefinitely if the inversion grows into the remainder of the shell. Thus, the energetics of the inversion dictates that the remainder collapses completely at $p_{c_2} = 0.22p_0$, which matches the point of collapse observed in numerical collapse simulations (Fig. 2). The loss of stability of the remainder of the shell, triggered by the merging of two fixed points in the energy curve, is analogous to a limit of metastability at a first order phase transition, and is classified as a *saddle-node bifurcation* in dynamical systems theory.[36]

To test this mechanism for loss of stability of the remainder, we analyzed the total energy $E_{tot}(d)$ from indentation simulations on shells with various cap sizes, to estimate the pressure at which the bifurcation occurs. This was compared to the pressure of collapse of the remainder as measured in pressure collapse simulations (Section III). The results are reported in Fig. 13(b). The estimates from indentation simulations agree quantitatively with the pressure collapse simulations for cap sizes down to $\lambda \approx 1$. The discrepancy for smaller cap sizes is to be expected—when the cap size is small compared to the elastic length scale of the shell, there is no separation of scales that lets us consider the stability of an inverted cap in the remainder of the shell. In that case, the deformations of the cap and the remainder are closely coupled and jointly determine the pressure of collapse of the shell.

B Dependence of collapse pressure on cap size and thickness

Having shown that stability considerations quantitatively determine p_{c_2} as a function of spot size for a particular value of the thickness ratio ($\tau = 0.4$), we now use scaling arguments to qualitatively understand how p_{c_2} changes with thickness ratio and cap size. Our previous estimate, $p_{c_2} = p_1(d_0) \sim p_0\gamma^{-1/4}\sqrt{R/d_0} \sim p_0/\lambda$ was inconsistent with the simulation results (Fig. 2) which show p_{c_2} approaching a constant value for large cap sizes rather than falling with cap size. (Recall that the cap height d_0 and the dimensionless cap size λ are related *via* $d_0 \approx R\lambda^2/2\sqrt{\gamma}$.) The previous estimate for p_{c_2} did not take into account the jump in the elastic energy $E_{el}(d)$ from $c\tau^{5/2}\kappa\gamma^{1/4}(d/R)^{3/2}$ to $c\kappa\gamma^{1/4}(d/R)^{3/2}$ when the inversion rim transitions from the cap into the remainder, which stabilizes the inversion of depth $d \approx d_0$ that arose due to the snap-through of the cap [see Fig. 12 and 13(a)]. This transition happens over some narrow depth range $d_0 \lesssim d \lesssim d_0 + \delta$, where δ is the depth change that causes the inversion rim radius $r \approx \sqrt{2dR}$ to increase from $r_0 = \sqrt{2d_0R}$ by an amount of order ℓ (*i.e.* the rim moved away from the cap boundary by an elastic length so that it no longer feels its influence). The required change in rim radius r corresponds to a depth change of order $\delta \sim \sqrt{d_0/R}\ell \sim \sqrt{d_0R}/\gamma^{1/4}$. The inversion of depth $d \approx d_0$ loses its stability when the jump in elastic energy is overcome by the pressure contribution, *i.e.* when $E_{tot}(d_0) \approx E_{tot}(d_0 + \delta)$. For $d_0 \gg \delta$, which corresponds to $\lambda \gg 1$ (the limit of large cap size), this criterion reduces to $c\kappa\gamma^{1/4}(d_0/R)^{3/2}(1 - \tau^{5/2}) \approx 4\pi pRd_0\delta$. Therefore, we expect the second buckling pressure p_{c_2} to scale as

$$p_{c_2} \sim \frac{\kappa\gamma^{1/4}(d_0/R)^{3/2}(1-\tau^{5/2})}{Rd_0\delta} \sim \frac{\kappa\sqrt{\gamma}(d_0/R)^{3/2}(1-\tau^{5/2})}{(Rd_0)^{3/2}} \sim p_0(1-\tau^{5/2}), \quad (73)$$

where we have used $p_0 = 4\sqrt{\kappa Y}/R^2 = 4\kappa\sqrt{\gamma}/R^3$ and $\delta \sim \sqrt{d_0R}/\gamma^{1/4}$. According to this estimate, the ratio p_{c_2}/p_0 is independent of cap size for large λ, consistent with the simulation results (Fig. 2). The predicted τ-dependence of the second buckling pressure is also consistent with the simulation results: the limiting value of p_{c_2} for large λ falls from $p_{c_2} = 0.23p_0$ for $\tau = 0.2$ to $p_{c_2} = 0.21p_0$ for $\tau = 0.4$, consistent with $p_{c_2}/p_0 \propto (1 - \tau^{5/2})$.

By combining this result for the loss of stability of the remainder with the results of the previous sections, we can now fully explain the buckling pathways summarized in Fig. 2. The (p_{c_1}/p_0) *vs.* λ curves, set by the snap-through of the cap, move to higher values of p/p_0 as τ increases, whereas the (p_{c_2}/p_0) *vs.* λ curves, set by the stability of the inverted cap against further growth into the remainder, move to lower values as τ increases [eqn (73)]. For $\tau \leq 0.4$, the former curve lies below the latter for

all values of λ, and two distinct buckling transitions are observed at p_{c_1} and p_{c_2} (pathway I) over a wide range of cap sizes. For $\tau \geq 0.6$, the cap snap-through pressures lie *above* the stability curve of the remainder, and an inverted cap is immediately unstable to growing into the remainder, leading to collapse of the whole shell at p_{c_1} (pathway II) for all cap sizes. The separate buckling pressure curves cross at thickness ratio $\tau = 0.5$, and shells with this thickness ratio buckle *via* either pathway I or pathway II, depending on the size of the soft region.

VIII Hysteresis

The buckling of uniform spherical shells is known to be *hysteretic* under cyclic changes in external pressure. A buckled shell with a large inversion re-inflates only when the pressure is brought down significantly below its buckling pressure p_0. This is illustrated in Fig. 14 for a numerical simulation on a uniform shell with $\gamma = 10^4$. The shell collapses close to p_0 (in practice, all simulated uniform shells buckle slightly below the classical buckling pressure because of the finite mesh and the non-uniformity in the mesh, to which the buckling transition is very sensitive), but only re-inflates when the pressure is brought down to about 10% of the buckling pressure.

This behavior can be understood from the Pogorelov scaling form [eqn (33)] for the elastic energy of an inversion, which we have already seen leads to an inflation pressure $p_I(d) \sim \gamma^{-1/4}\sqrt{R/d}\,p_0$ to re-inflate an inversion of depth d. In collapsed shells, the inversion depth is comparable the shell radius, and as a result $p_I \sim \gamma^{-1/4}p_0$ is very small compared to the buckling pressure for thin shells with $\gamma \gg 1$. In practice, this makes spherical buckled capsules difficult to re-inflate.

A large, thin soft region ($\tau < 0.5$, $\lambda \gtrsim 3$) mitigates hysteresis to some extent by bringing the buckling and re-inflation pressures closer to each other. Fig. 14 shows the volume evolution of a shell with $\tau = 0.4$ and $\lambda = 6.4$ ($\tilde{\lambda} = \lambda/\sqrt{\tau} = 10.1$), corresponding to a cap of height of $d_0 = 0.2R$. The shell follows buckling pathway I (a snap-through of the cap followed by buckling of the remainder at higher pressure, as in Fig. 1). The pressure of catastrophic collapse of the shell is brought down to $p_{c_2} = 0.22p_0$, and the shell re-inflates when the pressure is about a third of this value. The soft region also exhibits some hysteresis of its own, snapping back to its initial configuration at a pressure of $0.03p_0$ which is lower than the snap-through pressure $p_{c_1} = 0.13p_0$. This cap hysteresis is characteristic of the bistable state with two equilibrium solutions that is responsible for snap-through buckling (Fig. 4).

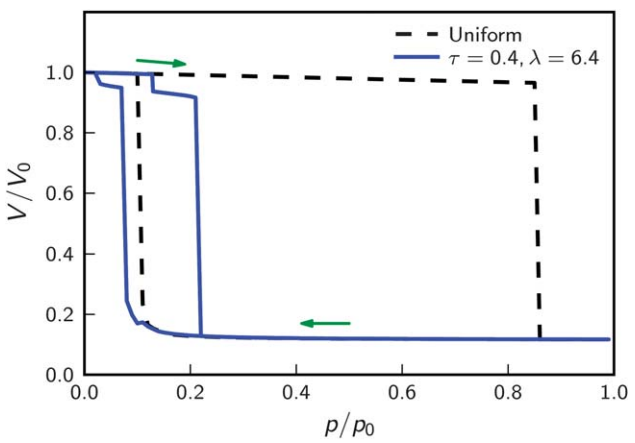

Fig. 14 Hysteresis loops for cyclical pressure variation on a shell without (dashed) and with (solid) a soft spot with $\tau = 0.4$ and $\lambda = 6.4$. In both cases, $\gamma = 10^4$. The curves show the evolution of the enclosed volume V, normalized by the initial volume $V_0 = 4\pi R^3/3$, as the pressure is first ramped up to $p = p_0$ and then back down to zero in steps of $\Delta p = 0.01p_0$.

These features may be exploited for applications that require shape changes of elastic capsules in response to changes in the pressure. First, the deflation and re-inflation pressures associated with large-scale collapse of the shell are brought much closer to each other for shells with soft spots (when $\tau < 0.4$), reducing the area of the hysteresis loop and making the shells more responsive to pressure cycling. Second, there is a wide range of parameters for which the soft spot can be inverted and re-inflated without collapsing the shell as a whole. This provides a mechanism for making capsules with a well-defined indentation (set by the cap size) that can be triggered or removed by changing the pressure. Such capsules could be used to make tunable "lock" colloids in a lock-and-key colloidal assembly system,[8] which may be induced to associate with, or be indifferent to, smaller "key" colloids depending on whether the cap is inverted to form a receptacle for the keys.

IX Conclusion

Our analysis shows that a circular thin region in a spherical shell, although a simple inhomogeneity to describe, strongly influences the buckling properties in important and subtle ways. By varying the thickness and size of the soft region, we can induce the shell to follow three different buckling pathways, each of which can be understood by analyzing the governing equations of the cap and the remainder. These pathways can be exploited to control the shell shapes swept out by varying the external pressure.

A wide range of buckling phenomena in inhomogeneous shells remains to be explored. It is already evident that the shape of the soft region[12] and the number of soft spots[13] fundamentally changes the buckling behavior; a systematic study of soft spots with non-circular shapes and of multiple soft spots on the same shell could uncover additional ways to control and exploit the buckling transition. We could also consider sectors on a shell with a different 3D elastic modulus E compared to the remainder, allowing us to vary the ratio of 2D Young's moduli $\tilde{Y}/Y$ independently from the ratio of bending rigidities $\tilde{\kappa}/\kappa$. Localized variations in the shell curvature, already studied in the context of imperfect shells,[37] may have interesting effects on the buckling properties as well. Inhomogeneities could likewise affect buckling pathways in other shell shapes known to buckle under external pressure, such as ellipsoids,[38] toroids,[39] and cylinders.[40] These and many more shell shapes and inhomogeneities can be explored using numerical simulations of the type used in this work.

Finally, we remark that a shell with a single soft region is likely to be less sensitive to imperfections in the shell shape

than a uniform shell. The sensitivity of the buckling transition to even minute deviations in the shell shape (of the order of the shell thickness) from the perfect sphere has already been mentioned. This sensitivity occurs because the mode responsible for buckling of a uniform shell (pictured in Fig. 3) is highly degenerate.[10] Since many such modes exist, it is likely that one or more of the modes couples strongly with the spatial shape variation, and acquires a non-zero amplitude (thus triggering shell collapse) at a pressure lower than the classical buckling pressure p_0 for a perfect shell. Depending on the strength of the coupling, the instability is triggered at a pressure that may be anywhere from 20–80% of p_0 for real-world shells, even if the deviations from the perfect sphere are only of the order of the thickness of the shell.[41] As a result, the true pressure at which uniform shells lose stability can be unpredictable. In contrast, the collapse of shells with thin soft spots ($\tau < 0.5$) is triggered by loss of stability of the snap-through state. As described in Section VII, this is governed by the energetics of nearly isometric inversions rather than the presence of highly degenerate modes. Since the scaling of the inversion energy with inversion depth is not sensitive to small imperfections, the buckling of the shell is expected to happen reliably at roughly $0.22p_0$ for large spots ($\lambda \gtrsim 4$), regardless of small deviations from the perfect shape. Even though the buckling pressure is greatly reduced by the soft spot, it can be known much more precisely. Paradoxically, introducing a known inhomogeneity in the shell thickness could make the buckling transition more reliable than for a uniform shell! This property could be exploited for applications, such as release of encapsulated materials under specific environmental conditions, that require precise control over the pressure at which buckling happens.

Appendix A: details of numerical simulation

For our simulations, we discretize the elastic energies on a floating mesh of 20 000 points. The initial mesh is disordered, with a distribution of nearest neighbor distances and a finite fraction of five-fold and seven-fold disclinations distributed throughout the mesh (Fig. 15). The disordered mesh approximates a shell made up of amorphous material, eliminating the 12 regularly spaced five-fold disclinations that inevitably arise when tiling a spherical surface with equilateral triangles.[42] The elastic stretching energy of deformations from the initial unstrained configuration is approximated by a harmonic spring energy associated with bonds connecting nearest-neighbor pairs:[43]

$$E_s = \sum_{\langle ij \rangle} \frac{\sqrt{3}}{4} Y \left(r_{ij} - r_{ij}^0 \right)^2 \tag{A1}$$

where r_{ij} and r_{ij}^0 are the lengths in the deformed and initial states of the bond connecting nearest-neighbor mesh points i and j. This form reproduces the stretching energy component of the elastic energy (eqn (5)) in the continuum limit, with $\nu = 1/3$.[43]

Previously used discretizations of the bending energy in terms of the angles between surface normals of adjacent facets in the mesh[12,43] are not suitable for disordered meshes.[44] Instead, we reconstruct the change in curvature k_{ij} from the mean curvature H_i and Gaussian curvature K_i estimated at each point i. This requires the discretized surface area A and enclosed volume V of the shell, obtained by treating the mesh as a polyhedron with planar triangular facets whose edges are the nearest-neighbor bonds. Each facet j contributes an area $A_j = |(\boldsymbol{r}_{j_2} - \boldsymbol{r}_{j_1}) \times (\boldsymbol{r}_{j_3} - \boldsymbol{r}_{j_1})|/2$, where $\boldsymbol{r}_{ji}$ ($i \in \{1,2,3\}$) are the position vectors of the three mesh points j_i that define the facet. The tetrahedron defined by the origin and the three vertices of each facet j contributes a signed volume $V_j = [\boldsymbol{r}_{j_1} \cdot (\boldsymbol{r}_{j_2} \times \boldsymbol{r}_{j_3})]/6$ to the total volume of the polyhedron. The contribution correctly calculates the enclosed volume of the mesh, provided the facet vertices j_1, j_2 and j_3 are ordered so that the vector $(\boldsymbol{r}_{j_2} - \boldsymbol{r}_{j_1}) \times (\boldsymbol{r}_{j_3} - \boldsymbol{r}_{j_1})$ points towards the outside of the shell. An estimate of the signed mean curvature at mesh point i is[45]

$$H_i = \frac{1}{2} \frac{\boldsymbol{F}_i \cdot \boldsymbol{N}_i}{\boldsymbol{N}_i \cdot \boldsymbol{N}_i} \tag{A2}$$

where $\boldsymbol{F}_i = \nabla_{\boldsymbol{r}_i} A$ is the gradient of the discretized surface area $A = \sum_j A_j$ with respect to $\boldsymbol{r}_i$, and $\boldsymbol{N}_i = \nabla_{\boldsymbol{r}_i} V$ is the gradient of the discretized volume $V = \sum_j V_j$. The Gaussian curvature at each point is estimated using the Gauss–Bonnet theorem:

$$K_i = \frac{1}{\sigma_i} \left(2\pi - \sum_{j(i)} \alpha_j \right) \tag{A3}$$

where α_j is the angle subtended by facet j at point i, and the sum is over all triangular facets sharing point i. $\sigma_i = \sum_{j(i)} A_j/3$ is the area associated with each vertex, computed as one-third of the sum of areas A_j of the facets $j(i)$ sharing point i. The discretized bending energy is[14]

$$E_b = \sum_i \frac{\kappa \sigma_i}{2} \left[4 \left(H_i - \frac{1}{R} \right)^2 - 2(1-\nu) \left(K_i - \frac{2H_i}{R} + \frac{1}{R^2} \right) \right]. \tag{A4}$$

The pressure is implemented by adding a term pV to the total energy. This net discretized energy $E_s + E_b + pV$ of the $3 \times 20\,000$ mesh points is then minimized using the BFGS quasi-Newton

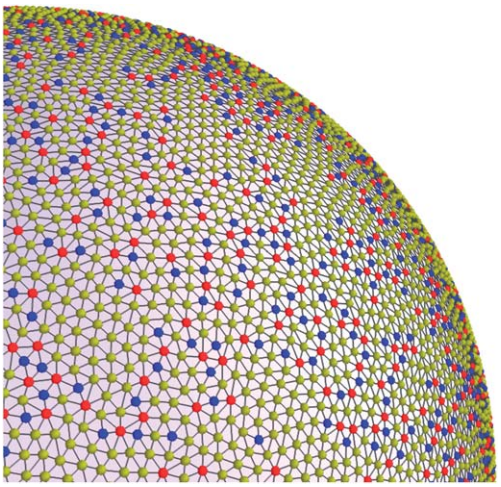

Fig. 15 Disordered mesh used in simulations. For clarity, only one octant of the mesh is shown. Mesh points are colored according to the number of nearest neighbors: blue (five neighbors), yellow (six neighbors) or red (seven neighbors); and nearest-neighbor pairs are connected by lines.

optimization algorithm, which finds local minima accessible smoothly from the initial state. We use the freely available GNU Scientific Library[46] to perform the minimization.

To simulate a solid inner ball centered at the origin (taken to be the center of the undeformed spherical shell) with a slightly smaller radius than the shell, we include a repulsive energy $E_{\rm rep} = \sum_i \varepsilon/(r_i - R_{\rm inner})^{12}$, where r_i is the distance of point i from the origin, and $R_{\rm inner} = 0.99R$ is the radius of the simulated inner ball. The strength $\varepsilon \sim 10^{-25}YR^2$ is kept very small so that points in the mesh only feel the influence of this repulsion when they are very close to the inner ball surface.

To minimize the errors introduced by using a discrete mesh with slight variations in near-neighbor bond lengths to simulate a smooth continuum shell, we ensure that the average length of near-neighbor bonds (which is $\langle r_{ij}^0 \rangle = 0.027R$ for the mesh used in our simulations, shown in Fig. 15) is smaller than the elastic length scales ℓ and $\tilde{\ell}$ for all the parameter values used. By repeating some of our simulations on meshes with 5000 and 13 392 points, and with different values of the Föppl–von Kármán number, we estimate that the reported buckling pressures for the simulated shells with sizeable soft spots are accurate to within $\pm 0.01 p_0$. Note that this is significantly smaller than the discrepancy between the buckling pressure of *uniform* shells (Fig. 14), or shells with extremely small spots ($\lambda < 0.5$ in Fig. 2), and the theoretical value. For reasons similar to those summarized in Section IX, simulations of shells with sizeable soft spots are likely to be less sensitive to the small scale inhomogeneities due to the disordered mesh than simulations of completely or nearly uniform shells.

Acknowledgements

We thank J. Hutchinson for helpful discussions on shell theory, F. Spaepen for pointing us towards relevant literature on elastic instabilities, E. Katifori and G. Vliegenthart for guidance with numerical simulations, S. Datta for general discussions, and the anonymous referees for constructive suggestions and corrections. We acknowledge support by the National Science Foundation *via* Grant DMR1005289 and through the Harvard Materials Research Science and Engineering Center *via* Grant DMR0820484.

References

1 L. Landau and E. Lifshitz, *Theory of Elasticity, Third Edition*, Butterworth-Heinemann, 1986.
2 A. M. A. van der Heijden, *W. T. Koiter's Elastic Stability of Solids and Structures*, Lecture notes compiled by the author, Cambridge University Press, 2009.
3 E. Katifori, S. Alben and D. R. Nelson, *Phys. Rev. E: Stat., Nonlinear, Soft Matter Phys.*, 2009, **79**, 056604.
4 D. Bushnell, *AIAA J.*, 1981, **19**, 1183.
5 A. Fery, F. Dubreuil and H. Möhwald, *New J. Phys.*, 2004, **6**, 18.
6 S. S. Datta, H. C. Shum and D. A. Weitz, *Langmuir*, 2010, **26**, 18612.
7 C. Quilliet, C. Zoldesi, C. Riera, A. van Blaaderen and A. Imhof, *Eur. Phys. J. E: Soft Matter Biol. Phys*, 2008, **27**, 13.
8 S. Sacanna, W. T. M. Irvine, P. M. Chaikin and D. J. Pine, *Nature*, 2010, **464**, 575.
9 M. A. Krenzke and R. M. Charles, *David Taylor Model Basin Report No. 1759*, 1963.
10 J. Hutchinson, *J. Appl. Mech.*, 1967, **34**, 49.
11 J. Paulose, G. A. Vliegenthart, G. Gompper and D. R. Nelson, *Proc. Natl. Acad. Sci. U. S. A.*, 2012, **109**, 19551.
12 E. Katifori, S. Alben, E. Cerda, D. R. Nelson and J. Dumais, *Proc. Natl. Acad. Sci. U. S. A.*, 2010, **107**, 7635.
13 J. Shim, C. Perdigou, E. R. Chen, K. Bertoldi and P. M. Reis, *Proc. Natl. Acad. Sci. U. S. A.*, 2012, **109**, 5978.
14 S. S. Datta, S.-H. Kim, J. Paulose, A. Abbaspourrad, D. R. Nelson and D. A. Weitz, *Phys. Rev. Lett.*, 2012, **109**, 134302.
15 T. Baumgart, S. T. Hess and W. W. Webb, *Nature*, 2003, **425**, 821.
16 S. L. Veatch and S. L. Keller, *Biophys. J.*, 2003, **85**, 3074.
17 G. Vernizzi, R. Sknepnek and M. Olvera de la Cruz, *Proc. Natl. Acad. Sci. U. S. A.*, 2011, **108**, 4292.
18 H. C. Shum, J.-W. Kim and D. A. Weitz, *J. Am. Chem. Soc.*, 2008, **130**, 9543.
19 A. Lazarus, H. C. B. Florijn and P. M. Reis, *Phys. Rev. Lett.*, 2012, **109**, 144301.
20 G. A. Vliegenthart and G. Gompper, *New J. Phys.*, 2011, **13**, 045020.
21 S. Knoche and J. Kierfeld, *Phys. Rev. E: Stat., Nonlinear, Soft Matter Phys.*, 2011, **84**, 046608.
22 N.-C. Huang, *J. Appl. Mech.*, 1964, **31**, 447.
23 D. Shilkrut, *Stability of Nonlinear Shells: On the Example of Spherical Shells*, Elsevier, Amsterdam, 2002.
24 Y. Park, C. A. Best, K. Badizadegan, R. R. Dasari, M. S. Feld, T. Kuriabova, M. L. Henle, A. J. Levine and G. Popescu, *Proc. Natl. Acad. Sci. U. S. A.*, 2010, **107**, 6731.
25 F. Niordson, *Shell Theory*, North-Holland, Amsterdam, 1986.
26 A. V. Pogorelov, *Bendings of surfaces and stability of shells*, American Mathematical Society, Providence, RI, 1988.
27 L. Pauchard and S. Rica, *Philos. Mag. B*, 1998, **78**, 225.
28 C. Quilliet, *Eur. Phys. J. E: Soft Matter Biol. Phys*, 2012, **35**, 1.
29 R. Carlson, R. Sendelbeck and N. Hoff, *Exp. Mech.*, 1967, **7**, 281.
30 E. Reissner, *J. Math. Phys.*, 1946, **25**, 80.
31 E. Reissner, *J. Math. Phys.*, 1946, **25**, 279.
32 B. Budiansky, *Proceedings of the Symposium on the Theory of Thin Elastic Shells*, North Holland Publishing Co., Amsterdam, 1969, p. 64.
33 D. Dubin, *Numerical and analytical methods for scientists and engineers using Mathematica*, Wiley-Interscience, 2003.
34 A. Vaziri and L. Mahadevan, *Proc. Natl. Acad. Sci. U. S. A.*, 2008, **105**, 7913.
35 B. Audoly and Y. Pomeau, *Elasticity and geometry: from hair curls to the non-linear response of shells*, Oxford University Press, 2010.
36 S. Strogatz, *Nonlinear dynamics and chaos*, Perseus Books Group, 2001.
37 T. Koga and N. J. Hoff, *Int. J. Solids Struct.*, 1969, **5**, 679.
38 J. R. Bar-On, R. J. Adams, J. Healey and B. Hyman, *AIAA J.*, 1967, **5**, 1469.

39 V. Yang and P. Jordan, *AIAA J.*, 1973, **11**, 1439.
40 V. Novozhilov, *The theory of thin elastic shells*, P. Noordhoff Ltd., Groningen, 1964.
41 W. Wunderlich and U. Albertin, *Int. J. Non Lin. Mech.*, 2002, **37**, 589.
42 J. Lidmar, L. Mirny and D. R. Nelson, *Phys. Rev. E: Stat., Nonlinear, Soft Matter Phys.*, 2003, **68**, 051910.
43 H. S. Seung and D. R. Nelson, *Phys. Rev. A: At., Mol., Opt. Phys.*, 1988, **38**, 1005.
44 G. Gompper and D. Kroll, *J. Phys. I*, 1996, **6**, 16.
45 K. A. Brakke, *Experiment. Math.*, 1992, **1**, 141.
46 M. Galassi, B. Gough, G. Jungman, J. Theiler, J. Davies, M. Booth and F. Rossi, *The GNU Scientific Library Reference Manual, Third Edition*, 2009.